PLOS BIOLOGY

RESEARCH ARTICLE

Preservation of developmental spontaneous activity enables early auditory system maturation in deaf mice

Calvin J. Kersbergen[1], Travis A. Babola[1,2], Patrick O. Kanold[2], Dwight E. Bergles[1,2,3,4]*

1 The Solomon H. Snyder Department of Neuroscience, Johns Hopkins University, Baltimore, Maryland, United States of America, **2** Department of Biomedical Engineering, Johns Hopkins University, Baltimore, Maryland, United States of America, **3** Department of Otolaryngology Head and Neck Surgery, Johns Hopkins University, Baltimore, Maryland, United States of America, **4** Kavli Neuroscience Discovery Institute, Johns Hopkins University, Baltimore, Maryland, United States of America

* dbergles@jhmi.edu

Citation: Kersbergen CJ, Babola TA, Kanold PO, Bergles DE (2023) Preservation of developmental spontaneous activity enables early auditory system maturation in deaf mice. PLoS Biol 21(6): e3002160. https://doi.org/10.1371/journal.pbio.3002160

Academic Editor: Alan G. Cheng, Stanford University, UNITED STATES

Received: December 5, 2022

Accepted: May 11, 2023

Published: June 27, 2023

Data Availability Statement: All relevant data is available within the manuscript and Supporting information files. Data and custom code for figure generation and analysis is available at: https://doi.org/10.5281/zenodo.7896212.

Funding: This work was supported by the National Institutes of Health (F30DC018711 to CJK, F32DC019842 to TAB, U19NS107464, R01DC009607 to POK, and R01DC008860, P30NS050274 to DEB.) The funders had no role in

Abstract

Intrinsically generated neural activity propagates through the developing auditory system to promote maturation and refinement of sound processing circuits prior to hearing onset. This early patterned activity is induced by non-sensory supporting cells in the organ of Corti, which are highly interconnected through gap junctions containing connexin 26 (*Gjb2*). Although loss of function mutations in *Gjb2* impair cochlear development and are the most common cause of congenital deafness, it is not known if these variants disrupt spontaneous activity and the developmental trajectory of sound processing circuits in the brain. Here, we show in a new mouse model of *Gjb2*-mediated congenital deafness that cochlear supporting cells adjacent to inner hair cells (IHCs) unexpectedly retain intercellular coupling and the capacity to generate spontaneous activity, exhibiting only modest deficits prior to hearing onset. Supporting cells lacking *Gjb2* elicited coordinated activation of IHCs, leading to coincident bursts of activity in central auditory neurons that will later process similar frequencies of sound. Despite alterations in the structure of the sensory epithelium, hair cells within the cochlea of *Gjb2*-deficient mice were intact and central auditory neurons could be activated within appropriate tonotopic domains by loud sounds at hearing onset, indicating that early maturation and refinement of auditory circuits was preserved. Only after cessation of spontaneous activity following hearing onset did progressive hair cell degeneration and enhanced auditory neuron excitability manifest. This preservation of cochlear spontaneous neural activity in the absence of connexin 26 may increase the effectiveness of early therapeutic interventions to restore hearing.

Introduction

Non-sensory supporting cells in the cochlea comprise a molecularly and physiologically diverse group of cells required for hearing. They secrete trophic factors critical for synapse development, remove neurotransmitters and ions generated through sound-evoked

study design, data collection and analysis, decision to publish, or preparation of the manuscript.

Competing interests: I have read the journal's policy and the authors of this manuscript have the following competing interests: DEB is a paid consultant of Decibel Therapeutics.

Abbreviations: ABR, auditory brainstem response; AC, auditory cortex; aCSF, artificial cerebrospinal fluid; DMEM, Dulbecco's modified Eagle's medium; DPOAE, distortion product otoacoustic emission; EP, endocochlear potential; FBS, fetal bovine serum; IC, inferior colliculus; IHC, inner hair cell; ISC, inner supporting cell; OHC, outer hair cell; ROI, region of interest; SGN, spiral ganglion neuron; SPL, sound pressure level.

mechanotransduction, and provide structural support to the sensory epithelium to enable amplification [1,2]. Despite their remarkable diversity, cochlear supporting cells are extensively coupled to each another through gap junctions, forming a functional syncytium to coordinate development of this complex structure and allow ionic and metabolic homeostasis to sustain hearing [3–7]. These intercellular channels consist primarily of the gap junction protein connexin 26 (Cx26) encoded by *Gjb2*. Although not directly involved in mechanotransduction or signal transmission from hair cells to spiral ganglion neurons (SGNs), mutations in *Gjb2* are the most prevalent cause of congenital non-syndromic hearing loss, accounting for >25% of all genetic hearing loss worldwide [8–10]. Prior studies revealed that loss of function variants in *Gjb2* impair the structural development of the cochlea and result in deafness [11–15]. Nevertheless, cochlear implants can restore hearing in children that lack Cx26 [16], suggesting that maturation of central auditory pathways occurs despite disruption of normal cochlear function during a critical period of development. However, the mechanisms that enable early maturation of brain circuits that process acoustic information despite these cochlear abnormalities have not been defined.

All sensory pathways that have been examined experience a period of early refinement dependent on input from peripheral sensory organs [17]. In the auditory system, spontaneous bursts of action potentials emerge from the cochlea prior to hearing onset (time of ear canal opening when there is a profound increase in sensitivity to airborne sound) and propagate throughout the developing central auditory pathway [18–23], inducing correlated firing of neurons that will later process similar frequencies of sound. This intrinsically generated activity is initiated by a group of inner supporting cells (ISCs) within the sensory epithelium that reside adjacent to inner hair cells (IHCs). Stochastic, spontaneous release of ATP from individual ISCs triggers a cascade of events that culminates in coordinated depolarization of nearby IHCs, eliciting highly stereotyped bursts of action potentials in SGNs in the absence of mechanosensation. In mouse, this period of burst firing continues for almost 2 weeks after birth, allowing auditory neurons to engage in experience-dependent plasticity to ensure proper processing of peripheral stimuli when the ear canal opens and acoustic sensitivity increases dramatically [17,24,25]. Disruption of Cx26-mediated communication during this period alters developmental programs in the cochlea, preventing formation of fluid-filled spaces around hair cells (e.g., tunnel of Corti and space of Nuel) [11,12]. It may also impair some forms of extracellular communication, as Cx26 can exist as an unpaired hemichannel at the cell surface to enable release of diverse signaling molecules, including ATP [26,27]. However, the effect of Cx26 deficiency on spontaneous neural burst firing has not been examined, and the consequences for maturation and refinement of auditory processing circuits within the brain remains poorly understood.

To understand how Cx26 deficiency influences both spontaneous burst firing in the cochlea and neuronal activity patterns in central auditory centers, we developed a new mouse model to achieve targeted, constitutive deletion of Cx26 (Cx26 cKO mice) from prehearing supporting cells within the organ of Corti, as global Cx26 deficiency is lethal [28]. Cx26 cKO mice exhibited a profound loss of acoustic sensitivity at ear canal opening (P11) and progressive cellular degeneration within the cochlea, consistent with evidence that supporting cell coupling within the cochlea is required for normal hearing. However, ISCs in cochleae from prehearing Cx26 cKO mice unexpectedly retained low membrane resistance, intercellular dye coupling, and spontaneous electrical activity mediated by ATP release. These ISCs also continued to induce coordinated activation of IHCs along the length of the cochlea, excitation of SGNs, and correlated firing of auditory neurons within isofrequency zones in vivo. Although auditory neurons in the midbrain and cortex after ear canal opening were only activated in Cx26 cKO mice by very loud sounds, their spatial and temporal neuronal activity patterns were remarkably

similar to controls. With increasing age, cortical neuron responses to sound in Cx26 cKO mice became larger and more prolonged, suggesting an adaptive response to the lack of input after cessation of spontaneous activity. These results reveal that patterned neural activity is preserved during development in the absence of Cx26, enabling activity-dependent maturation of auditory circuits and homeostatic control of acoustic sensitivity despite later deafness, helping to establish appropriate neural networks in the brain that can be engaged by cochlear prostheses.

Results

Targeted deletion of Cx26 from the cochlear sensory epithelium leads to auditory dysfunction

Non-sensory supporting cells in the organ of Corti maintain electrical and chemical coupling through gap junctions, which have been implicated in generating spontaneous activity prior to hearing onset by enabling transfer of second messengers between cells [29–31] and ATP release when present as unpaired hemichannels at the cell surface [18,26]. To determine how selective loss of Cx26 from these supporting cells influences spontaneous activity before hearing onset and later auditory function, we bred *Gjb2*$^{fl/fl}$ mice [11] to *Tecta-Cre* mice (*Tecta-Cre; Gjb2*$^{fl/fl}$, Cx26 cKO), which exhibit recombination within the embryonic cochlear sensory epithelium and limited recombination in central auditory nuclei [32–34]. Immunohistochemical analysis of cochleae from these mice revealed that the large Cx26 gap junction plaque assemblies separating supporting cells in the mature sensory epithelium were eliminated (Fig 1a and 1b, white arrows); however, Cx26 expression was preserved in the outer sulcus, spiral limbus, lateral wall fibrocytes, and stria vascularis (Fig 1b, green arrows), consistent with the restricted expression of *Tecta* (α-Tectorin) [34]. Thus, these conditional Cx26 knockout mice provide a means to explore the specific role of Cx26 within the cochlear sensory epithelium.

To determine if loss of Cx26 from the sensory epithelium is sufficient to disrupt cochlear function and hearing, we recorded auditory brainstem responses (ABRs) and distortion product otoacoustic emissions (DPOAEs) at P21, when normal auditory function has been established. Cx26 cKO mice exhibited profound hearing deficits (Fig 1c and 1d), with ABR threshold increases of approximately 50 to 60 dB to both clicks and pure tones relative to controls, in accordance with hearing loss described in mouse models with widespread cochlear Cx26 deletion [12,35,36] and children with loss of function variants in Cx26 [13,14]. Cx26 cKO mice exhibited near-complete loss of DPOAEs at all tested frequencies (Fig 1e and 1f) indicating that outer hair cell (OHC) function and cochlear amplification are compromised. However, acoustic sensitivity was not abolished in Cx26 cKO mice, as low amplitude ABRs were still elicited at high sound intensities (>80 dB sound pressure level (SPL)), suggesting that mechanotransduction and excitation of SGNs is still possible at this age. These results indicate that removal of Cx26 specifically from supporting cells of the sensory epithelium is sufficient to impair hearing.

Despite this evidence of profound auditory dysfunction, the cochlea in Cx26 cKO mice was largely intact at an age when acoustic sensitivity is normally mature (@P21). The most prominent structural abnormalities in the sensory epithelium were the absence of the tunnel of Corti and Nuel's space, resulting in a flattening of the sensory epithelium, as well as subtle morphological changes in hair cell orientation and spacing (Fig 1a and 1g and 1h), features also observed in mice with broader Cx26 deletion [12,37]. While no hair cell degeneration was observed prior to ear canal opening (S2 Fig), partial OHC loss was evident throughout the cochlear length by P21, occurring first in the base (Figs 1a and S2 and S3a and S3b, white arrows) that became more extensive with age, although this cell loss was lower than reported

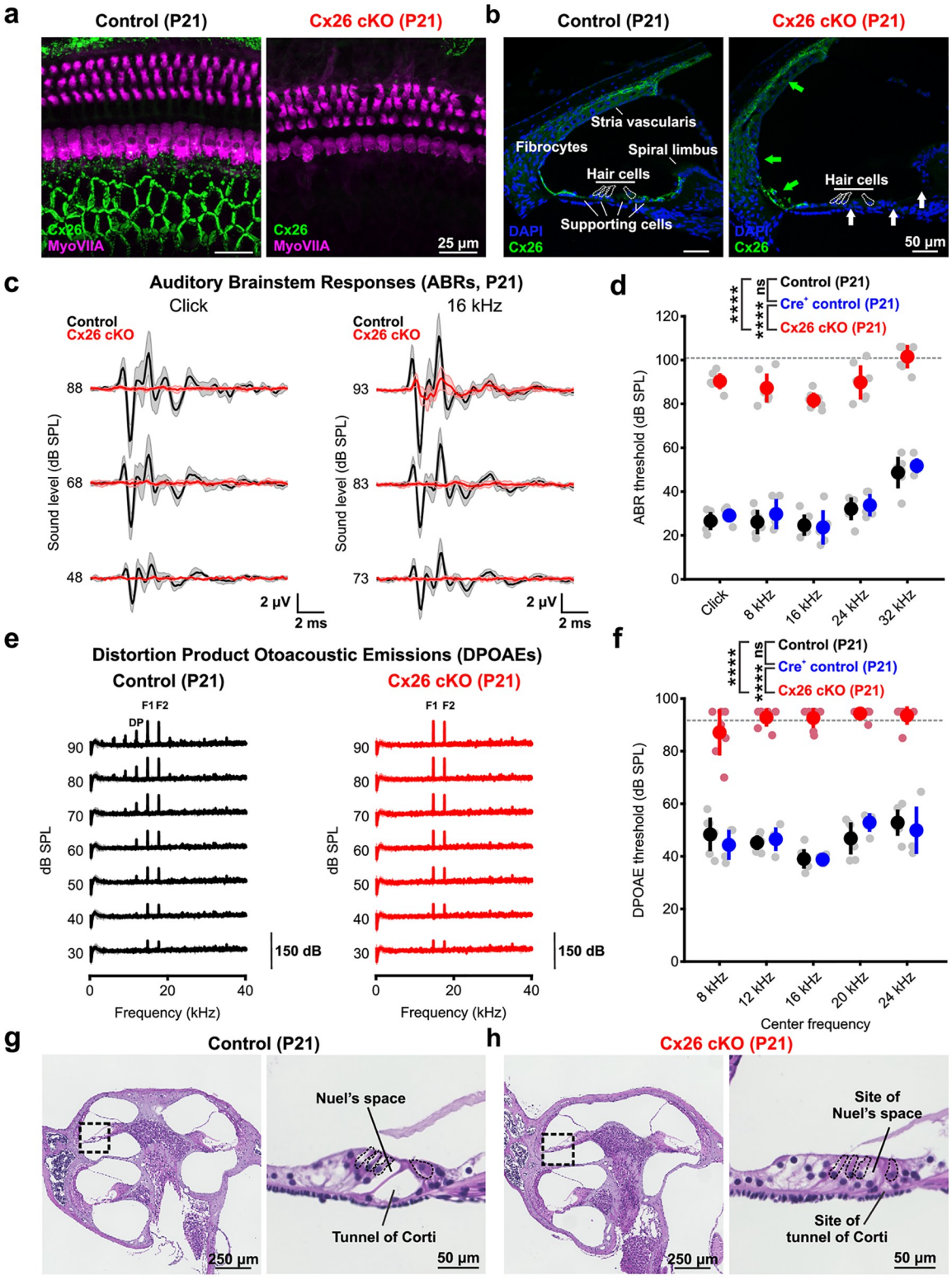

Fig 1. Targeted deletion of Cx26 from the sensory epithelium leads to auditory dysfunction. (a) Immunostaining for Connexin 26 (green) in whole mount apical cochlea from P21 control (*Gjb2*$^{fl/fl}$, left) and Cx26 cKO (*Tecta-Cre;Gjb2*$^{fl/fl}$, right) mice. Hair cells (magenta) are labeled by immunoreactivity against MyoVIIA. (b) Immunostaining for Connexin 26 (green) in mid-turn cochlea cross section at P21 from control (left) and Cx26 cKO (right) mice. Loss of Cx26 immunostaining is observed in the inner sulcus and supporting cells of the organ of Corti (white arrows) but not within lateral wall fibrocytes or the stria vascularis (green arrows). Hair cell

bodies are outlined based on nuclei (DAPI) location. (c) Average ABR traces to broadband click (left) and 16 kHz tone pip (right) stimuli presented at multiple SPLs from control (*Gjb2*$^{fl/fl}$, black, $n = 6$) and Cx26 cKO (*Tecta-Cre;Gjb2*$^{fl/fl}$, red, $n = 7$) mice at P21. (d) Quantification of P21 ABR thresholds to click and pure tone stimuli in controls (*Gjb2*$^{fl/fl}$, black, $n = 6$, *Tecta-Cre;Gjb2*$^{fl/+}$, blue, $n = 5$) and Cx26 cKO (*Tecta-Cre;Gjb2*$^{fl/fl}$, red, $n = 7$). Gray dashed line indicates maximum speaker output and detection limit. $p = 3.4380e\text{-}13$ (cKO vs. control), 1.2801e-9 (cKO vs. Cre+ control), 0.4774 (control vs. Cre+ control), linear mixed effects model. (e) Average recording of DPOAEs for a 16 kHz center frequency at multiple SPLs from control (*Gjb2*$^{fl/fl}$, black, $n = 7$) and Cx26 cKO (*Tecta-Cre;Gjb2*$^{fl/fl}$, red, $n = 7$) mice at P21. F1; primary tone 1 (14.544 kHz), F2; primary tone 2 (17.440 khz), DP; distortion product. (f) Quantification of distortion product thresholds for 5 center frequencies in controls (*Gjb2*$^{fl/fl}$, black, $n = 7$ and *Tecta-Cre;Gjb2*$^{fl/+}$, blue, $n = 4$) and Cx26 cKO (*Tecta-Cre;Gjb2*$^{fl/fl}$, red, $n = 7$). Gray dashed line indicates maximum speaker output and detection limit. $p = 2.3326e\text{-}14$ (control vs. cKO), 4.7233e-10 (Cre+ control vs. cKO), 0.9759 (control vs. Cre+ control), linear mixed effects model. (g) (Left) Hematoxylin and eosin stain of mid-modiolar section of a P21 control cochlea. Black square indicates site of high magnification. (Right) Magnified image of the organ of Corti, with the tunnel of Corti and Nuel's space indicated. (h) (Left) Hematoxylin and eosin stain of mid-modiolar section of a P21 Cx26 cKO cochlea. Black square indicates site of high magnification. (Right) Magnified image of the organ of Corti, with site of the tunnel of Corti and Nuel's space indicated. Analysis code, plotted figure panels, and statistical analysis can be found at: https://doi.org/10.5281/zenodo.7896212. ABR, auditory brainstem response; DPOAE, distortion product otoacoustic emission; SPL, sound pressure level.

https://doi.org/10.1371/journal.pbio.3002160.g001

with cochlea-wide deletion [35,36]. Remarkably, there was no notable degeneration of IHCs and SGNs at P21 in Cx26 cKO mice (S3b–S3d Fig). Progressive degeneration of IHCs eventually occurred with increasing age in a base-apex progression (S2 Fig). Together, these results demonstrate that selective deletion of Cx26 from supporting cells in the sensory epithelium leads to structural abnormalities in the cochlea and progressive hair cell degeneration following hearing onset.

ISCs continue to generate spontaneous activity in the absence of Cx26

Supporting cells in the developing cochlea express several distinct gap junction proteins, most prominently Cx26 and Cx30, which can form intercellular channels and uncoupled hemichannels at the cell surface. Notably, expression of these 2 gap junctions is closely linked and disruption of Cx26 has been shown to disrupt Cx30 expression, and vice versa [35,38–40]. To determine how loss of Cx26 affects the physiological properties and intercellular coupling of ISCs, we made whole cell patch clamp recordings from ISCs in cochleae acutely isolated at P7, targeting cells in the lateral region of Kölliker's organ that are responsible for generating spontaneous activity [18,19] (Figs 2a and S4a and S4b). ISCs in control cochleae exhibited both low membrane resistance (16.9 ± 5.2 MΩ) (Fig 2b) and extensive coupling, visible as the diffuse spread of tracer throughout Kölliker's organ [3] (Fig 2c, green fluorescence). Unexpectedly, ISCs in Cx26 cKO mice also exhibited extensive tracer spread (Fig 2d–2f) and retained low membrane resistance (22.3 ± 4.1 MΩ) (Fig 2f), indicating that they remain coupled through gap junctions; however, tracer movement was more restricted, with less diffusion within Kölliker's organ and between inner phalangeal cells and inner pillar cells. Preserved coupling in ISCs was not mediated by Cx30 gap junctions at P7, as Cx26 cKO ISCs exhibited a dramatic reduction and developmental delay in the appearance of Cx30 immunoreactive plaques (S4c–S4e Fig). Thus, even in the absence of Cx26 (and Cx30), ISCs in the developing cochlear epithelium remain coupled through gap junctions.

ISCs exhibit spontaneous electrical activity from the late embryonic period through ear canal opening, after which it rapidly disappears. This spontaneous activity is initiated by periodic release of ATP and activation of metabotropic P2RY1 autoreceptors on ISCs, eliciting calcium release from intercellular stores and opening of the calcium-activated chloride channel TMEM16A [41,42]. Prior studies suggests that the frequency and spatial spread of spontaneous calcium transients throughout the GER is reduced but not eliminated in Cx30 null mice that have residual Cx26 expression [43,44]. To explore how the absence of Cx26 influences ISC activity prior to hearing onset, we recorded spontaneous activity patterns from ISCs (Fig 2a)

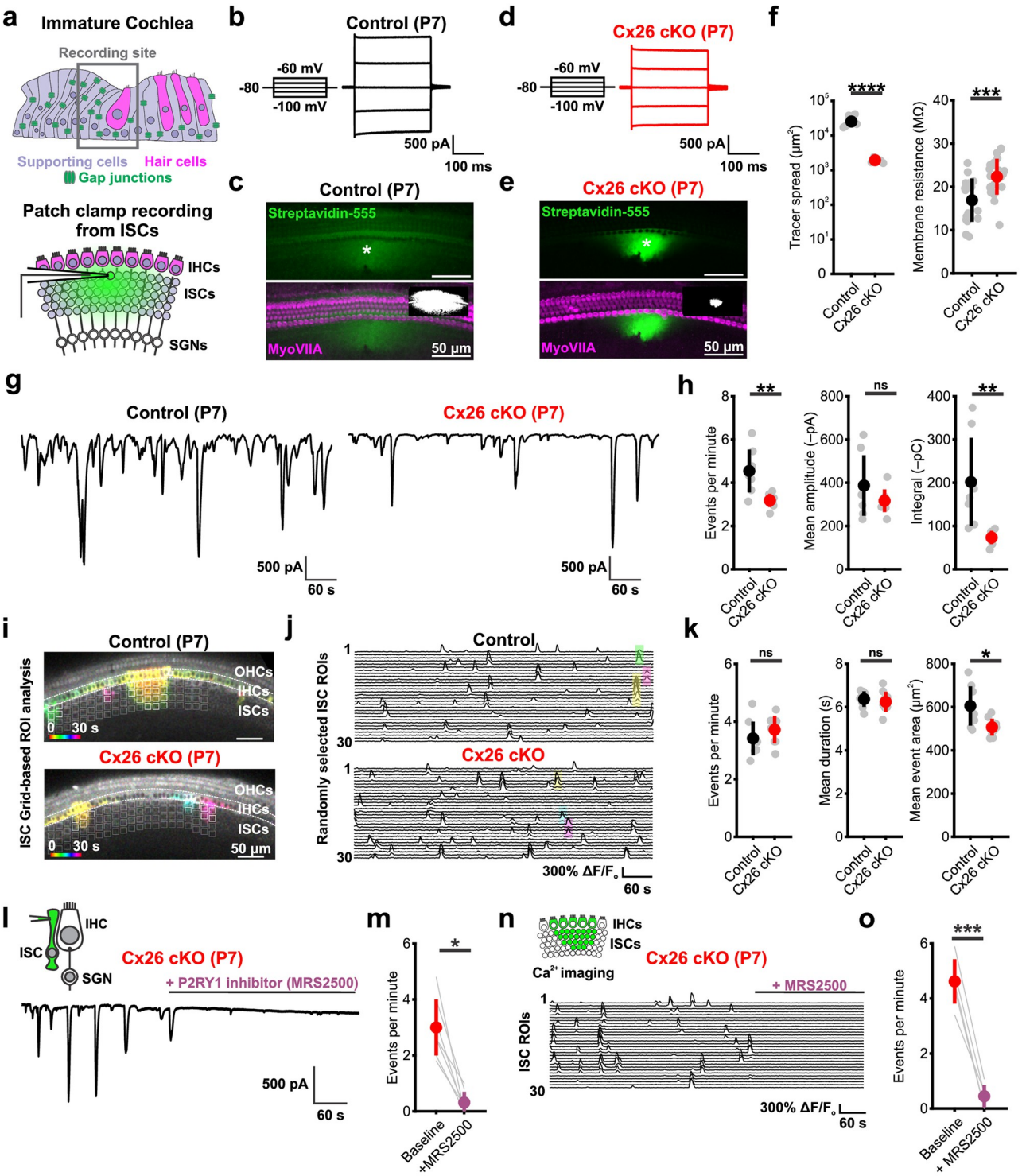

Fig 2. ISCs generate spontaneous activity in the absence of Cx26. (a) (Top) Schematic depicting cross section of the immature cochlea with targeted recording site for electrophysiology and calcium imaging from ISCs indicated. (Bottom) Schematic of whole cell patch clamp recording from ISCs in whole mount cochlea with an intercellular tracer within the pipette. IHC: inner hair cell; SGN: spiral ganglion neuron. (b) Current responses elicited by voltage steps within a P7 control ($Gjb2^{fl/fl}$) ISC. (c) (Top) Visualization of intercellular Neurobiotin tracer spread from a P7 control ISC with fluorescent conjugated streptavidin (green). Asterisk indicates patched cell. (Bottom) Same as above, but with hair cells labeled by immunoreactivity to Myosin VIIa (magenta) and binarized tracer spread for quantification in inset. (d) Current responses elicited by voltage steps within a P7 Cx26 cKO (*Tecta-Cre; $Gjb2^{fl/fl}$*) ISC. (e) Same as (c), but in a Cx26 cKO cochlea. (f) Quantification of spatial tracer spread (left) and membrane resistance (right) in ISCs. Tracer spread: $n = 4$ control, 6 Cx26 cKO cochleae; $p = 2.1864e\text{-}8$, two-sample t test. Membrane resistance: $n = 17$ control, 24 Cx26 cKO ISCs;

p = 6.3712e-4, two-sample t test. (g) Whole cell voltage clamp recordings of spontaneous activity from control (left) and Cx26 cKO (right) ISCs. (h) Quantification of spontaneous event frequency, mean amplitude, and integral (charge transfer). N = 7 control, 8 Cx26 cKO ISCs; p = 0.0045, 0.2405, 0.0061 (frequency, amplitude, and integral), two-sample t test with unequal variances and Benjamini–Hochberg correction for multiple comparisons. (i) Temporally pseudocolored 30 s projection of spontaneous calcium transients in ISCs from isolated prehearing cochlea from P7 control (*Tecta-Cre;Gjb2*$^{fl/+}$;*R26-lsl-GCaMP3*, top) and Cx26 cKO (*Tecta-Cre;Gjb2*$^{fl/fl}$;*R26-lsl-GCaMP3*$^{fl/+}$, bottom) mice. Grid-based ROI analysis is overlaid, with active grids during the 30 s window indicated in white. (j) Raster plot of $\Delta F/F_o$ signals from 30 randomly selected grid ROIs in control (top) and Cx26 cKO (bottom) cochleae. Highlighted transients correspond by color to those indicated in (f). (k) Quantification of ISC calcium event frequency (per 0.01 mm^2), mean duration, and mean event area. n = 8 control, 9 Cx26 cKO; p = 0.3080, 0.5683, 0.0140 (frequency, duration, and area), two-sample t test with Benjamini–Hochberg correction. (l) Whole cell voltage clamp recording from a P7 Cx26 cKO ISC with addition of P2RY1 receptor antagonist MRS2500 (1 μM). (m) Quantification of spontaneous event frequency at baseline and following P2RY1 antagonist. N = 7 Cx26 cKO ISCs; p = 0.0156, paired Wilcoxon sign rank test. (n) Raster plot of calcium $\Delta F/F_o$ signals from 30 randomly selected ISC grid ROIs from a Cx26 cKO cochlea with addition of MRS2500. (o) Quantification of mean event frequency (per 0.01 mm^2) at baseline and following P2RY1 antagonism. n = 5 Cx26 cKO cochlea; p = 3.0798e-4, paired t test. Analysis code, plotted figure panels, and statistical analysis can be found at: https://doi.org/10.5281/zenodo.7896212. ISC, inner supporting cell; ROI, region of interest.

https://doi.org/10.1371/journal.pbio.3002160.g002

using whole cell recording and imaged intracellular calcium changes from the cochlear sensory epithelium in acutely excised cochleae from P7 mice lacking Cx26. Periodic inward currents were still visible in ISCs from Cx26 cKO mice, but they were less frequent and shorter in duration than in controls, leading to less overall charge transfer (integral of the current trace) (Fig 2g and 2h). These reductions are consistent with impaired electrical coupling, as activity throughout the supporting cell syncytium is detected when recording from individual cells [3]. Calcium imaging in the cochlea (*Tecta-Cre;Rosa26-lsl-GCaMP3* ± *Gjb2*$^{fl/fl}$) [45] revealed that spontaneous ISC calcium transients from P7 Cx26 cKO cochlea occurred at a similar frequency as controls, and had a comparable average duration, but extended over a slightly smaller area along both medial-lateral and tonotopic axes (Fig 2i–2k, S1 Video). Both inward currents and calcium transients in Cx26 cKO cochleae were blocked by MRS2500 (1 μM) [32], a P2RY1 selective antagonist (Fig 2l–2o), indicating that ISCs release ATP and initiate a P2RY1-mediated signaling cascade in the absence of Cx26. Moreover, osmotic shrinkage (crenation) of ISCs, which follows ATP-dependent ion efflux [19], was also evident in Cx26 cKO ISCs (S5a Fig). The average spread of these osmotic crenations was reduced in Cx26 cKO cochleae, consistent with the reduced extent of ISC calcium transients along the tonotopic axis (Figs 2k and S5b). Together, these data indicate that key features of ISC spontaneous activity in the developing cochlea (ATP release, coordinated calcium transients, and ionic flux from ISCs) are preserved when Cx26 is absent from the supporting cell gap junction network.

ISCs coordinate excitation of IHCs and SGNs in the absence of Cx26

In the developing cochlea, ISC-mediated extrusion of potassium leads to depolarization and synchronous excitation of nearby IHCs within a restricted region of the organ of Corti [19,42]. To determine whether ISCs in Cx26 cKO mice remain capable of eliciting IHC depolarization, we monitored the spontaneous activity of IHCs in acutely isolated P7 cochleae (Fig 3a). Consistent with persistence of large ATP-induced inward currents in ISCs, IHCs in Cx26 cKO mice exhibited spontaneous inward currents at a frequency and amplitude comparable to controls (Fig 3b–3d). In accordance with the briefer ISC events, IHC events were also shorter in duration, leading to a decrease in total charge transfer (integral) per event (Fig 3d). This spontaneous activity in IHCs was similarly dependent on ISC ATP release, as it was abolished by MRS2500 (Fig 3e and 3f). Notably, the physiological properties of IHCs (current-voltage relationship, resting membrane potential, and input resistance) were comparable between control and Cx26 cKO mice (S6 Fig), suggesting that these subtle changes in IHC spontaneous currents are due to extrinsic changes in supporting cell ion flux surrounding IHCs.

As fewer ISCs are activated by each ATP release event in Cx26 cKO cochleae (Fig 2k) and currents induced in IHCs had less charge transfer, we hypothesized that this may result in

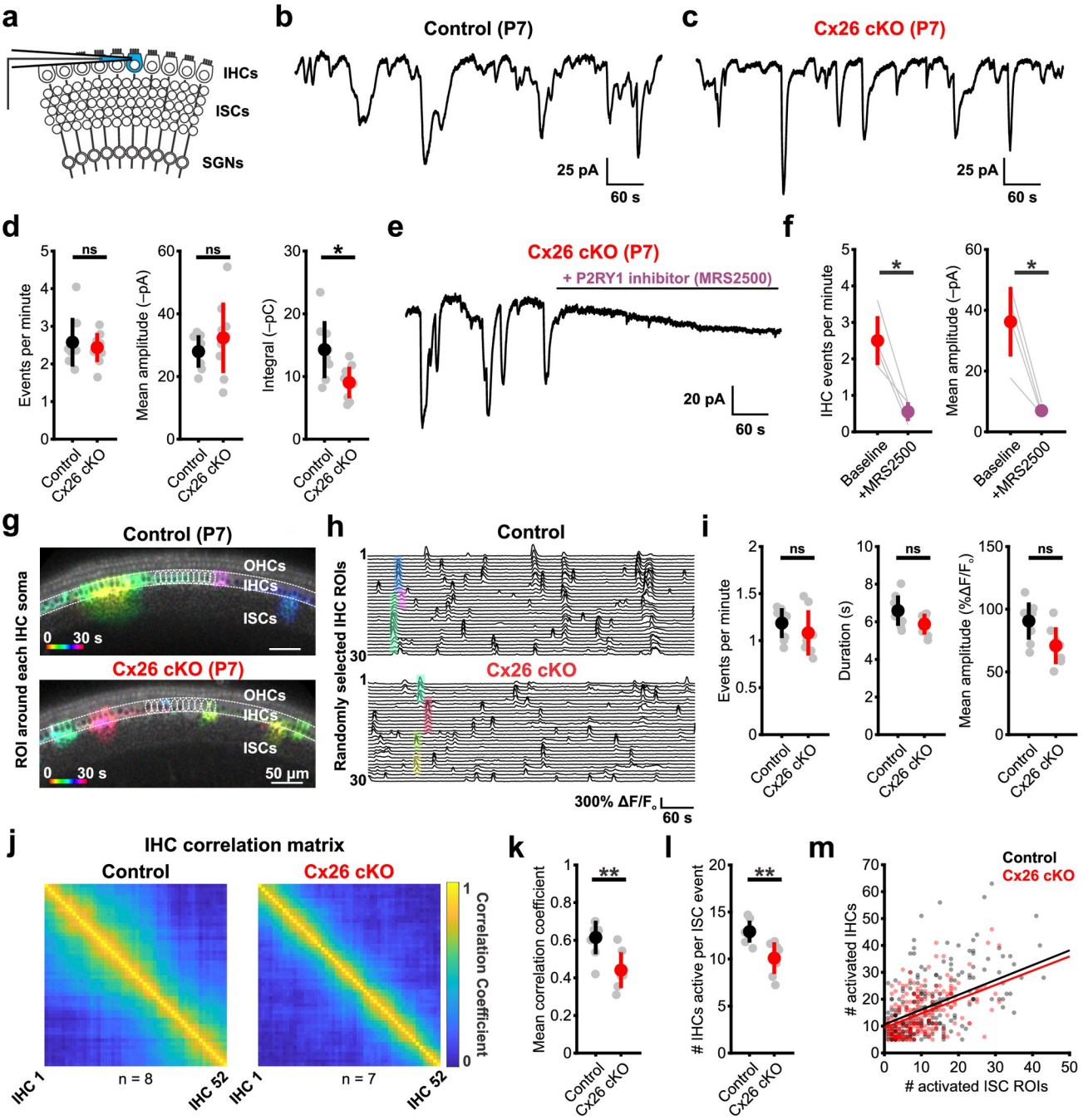

Fig 3. ISCs coordinate excitation of IHCs despite absence of Cx26. (a) Schematic of whole cell patch clamp recordings from IHCs. (b) Representative whole cell voltage clamp trace of spontaneous activity from a control (*Gjb2*$^{fl/fl}$) IHC. (c) Representative whole cell voltage clamp trace of spontaneous activity from a Cx26 cKO (*Tecta-Cre;Gjb2*$^{fl/fl}$) IHC. (d) Quantification of spontaneous inward current frequency, mean amplitude, and integral (charge transfer). $N = 8$ control, 9 Cx26 cKO IHCs; $p = 0.9626, 0.3587, 0.0134$ (frequency, amplitude, and integral), two-sample t test with Benjamini–Hochberg correction. (e) Whole cell voltage clamp recording from a Cx26 cKO IHC with addition of P2RY1 receptor antagonist MRS2500 (1 μM). (f) Quantification of spontaneous inward current frequency and mean amplitude in IHCs before and following addition of MRS2500. $N = 4$ Cx26 cKO IHCs; $p = 0.0132, 0.0168$ (frequency, amplitude), paired t test with Benjamini–Hochberg correction. (g) Temporally pseudocolored 30 s projection of spontaneous calcium transients in IHCs in isolated prehearing cochlea from control (*Tecta-Cre; Gjb2*$^{fl/+}$*;R26-lsl-GCaMP3*, top) and Cx26 cKO (*Tecta-Cre; Gjb2*$^{fl/fl}$*;R26-lsl-GCaMP3*, bottom) mice. Individual IHC oval ROIs are overlaid. (h) Raster plot of $\Delta F/F_o$ signals from 30 randomly selected IHCs in control (top) and Cx26 cKO (bottom) cochleae. Highlighted transients correspond by color to those indicated in (g). (i) Quantification of mean IHC calcium event frequency, duration, and amplitude. $n = 8$ control, 7 Cx26 cKO cochleae; $p = 0.4634, 0.1158, 0.0648$ (frequency, duration, and amplitude). Wilcoxon rank sum test (frequency) or two-sample t test (duration, amplitude) with Benjamini–Hochberg correction. (j) Mean correlation matrix of IHC $\Delta F/F_o$ signals in control (left) and Cx26 cKO (right) cochleae. (k) Quantification of mean correlation coefficient (80th percentile) between IHCs. $n = 7$

control, 7 Cx26 cKO cochleae; $p = 0.0048$, two-sample t test. (l) Quantification of mean number of IHCs active per supporting cell calcium event. $N = 7$ control, 7 Cx26 cKO cochleae; $p = 0.0057$, two-sample t test. (m) Scatter plot of activated ISC grid ROIs and activated IHCs during supporting cell calcium events in control (gray) and Cx26 cKO (pink) cochleae. Solid line indicates linear regression model of group data in control (black) and Cx26 cKO (red). Analysis code, plotted figure panels, and statistical analysis can be found at: https://doi.org/10.5281/zenodo.7896212. IHC, inner hair cell; ISC, inner supporting cell; ROI, region of interest.

https://doi.org/10.1371/journal.pbio.3002160.g003

more spatially restricted activation of IHCs. Calcium imaging revealed that transients within individual IHCs occurred at a similar rate in control and cKO cochlea, and the duration and amplitude of these events were not statistically different, although they trended lower (Duration: $p = 0.12$; Amplitude: $p = 0.065$; two-sample t test with Benjamini–Hochberg FDR correction) (Fig 3h and 3i). IHC activity correlation matrices revealed that the extent of synchrony was lower in Cx26 cKO cochleae (Fig 3j and 3k), with approximately 20% fewer IHCs activated per ISC calcium transient (Fig 3l). This reduction in IHC activity in Cx26 cKO mice was highly correlated with the extent of ISC activation, as linear regression fits to the number of IHCs and ISCs activated per event had comparable slopes (Fig 3m), suggesting that the reduction in spread of activity among ISCs in Cx26 cKO mice, and thus the area from which potassium is released, leads to fewer IHCs being depolarized.

IHCs in the developing cochlea are excitable and can generate calcium action potentials upon depolarization, bursts of which result in glutamate release onto SGN afferent fibers, activation of AMPA and NMDA receptors, depolarization, and burst firing [21,46]. To determine if synaptic connectivity between IHCs and SGNs is preserved in the absence of Cx26, we monitored SGN activity using calcium imaging in excised P7 cochlea from control (*Gjb2*$^{fl/fl}$; *Snap25-T2A-GCaMP6s*) and Cx26 cKO mice (*Tecta-Cre;Gjb2*$^{fl/fl}$;*Snap25-T2A-GCaMP6s*) [47] (Fig 4a). In cochleae from Cx26 cKO mice, spontaneous calcium transients occurred periodically among groups of SGNs located within spatially restricted regions of the cochlea at similar rates and duration as controls, but with reduced correlation (Fig 4b–4d). SGN calcium transients in Cx26 cKO cochleae were similarly dependent on synaptic excitation by IHCs, as they were blocked by the AMPA-receptor antagonist NBQX (50 μM) (Fig 4e and 4f and S2 Video). Electrical activity of SGNs during this critical period of development has been shown to influence both the maturation and survival of SGNs [48–50]; consistent with preservation of activity, Tuj1 immunoreactivity revealed that SGNs in P7 Cx26 cKO mice were present in numbers comparable to control mice (Fig 4g and 4h). Together, these results indicate that there is unexpected preservation of IHC-SGN synaptic coupling and patterned spontaneous activity in the cochleae of Cx26 cKO mice prior to hearing onset, resulting in coordinated activation of neurons that project to central auditory centers.

Spontaneous activity persists in the developing auditory system of Cx26 cKO mice

Action potential bursts generated in SGNs propagate along the ascending auditory pathway with remarkable fidelity, inducing correlated firing of neurons within isofrequency zones in central auditory centers [21–23]. In the inferior colliculus (IC), this ascending input manifests as discrete bands of neuronal activity aligned to the future tonotopic axis [22,51]. To determine if the correlated firing of auditory neurons within these lamina is affected in Cx26 cKO mice, we performed widefield neuronal calcium imaging in awake, unanesthetized mice (*Gjb2*$^{fl/fl}$; *Snap25-T2A-GCaMP6s* and *Tecta-Cre;Gjb2*$^{fl/fl}$;*Snap25-T2A-GCaMP6s*) through a cranial window placed over the midbrain (Fig 5a). Consistent with persistence of SGN burst firing in P7 Cx26 cKO mice, temporally and spatially correlated bands of neuronal activity were observed within discrete domains of the IC, resembling patterns observed in controls (Figs 5b and S7a–

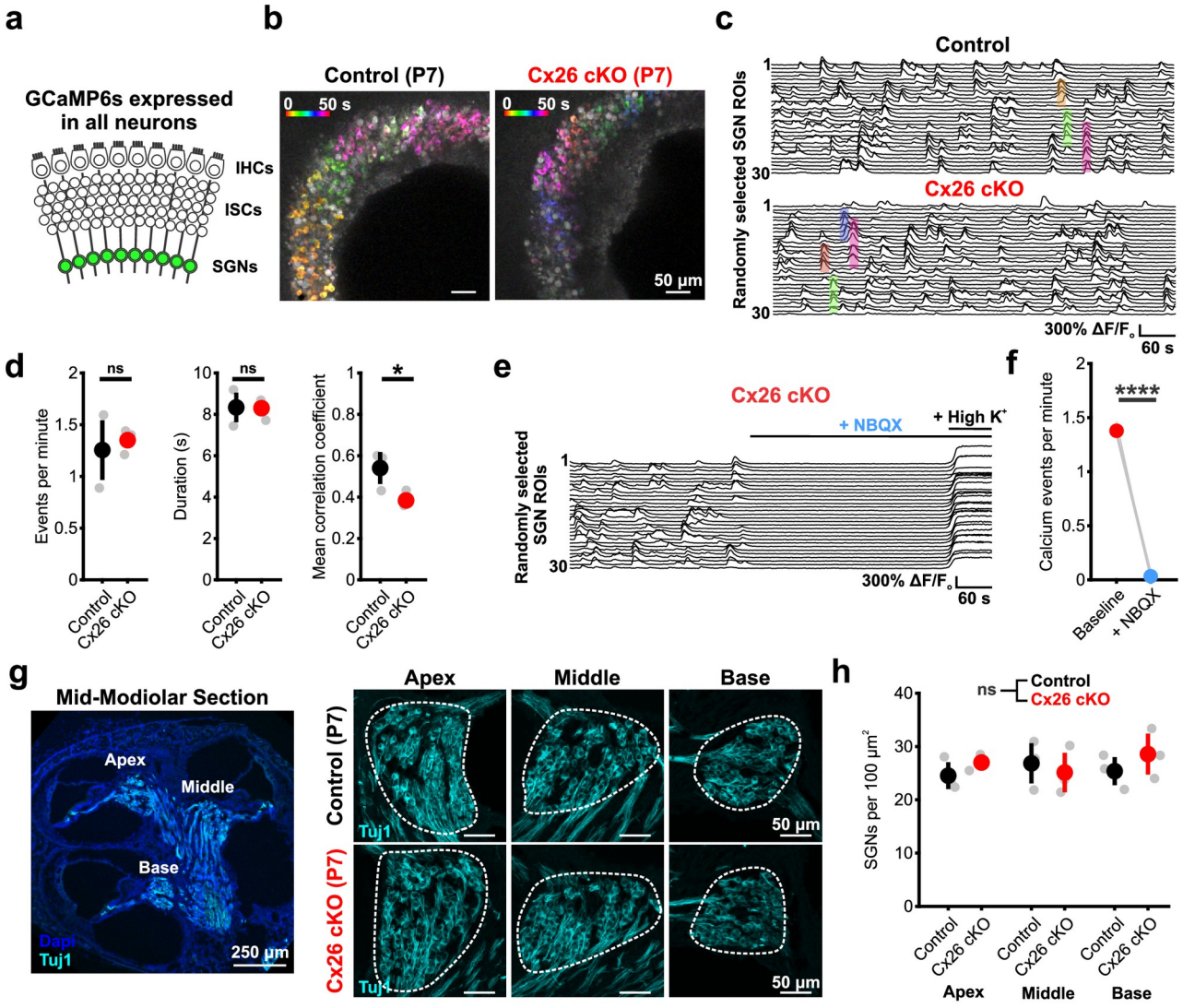

Fig 4. Spontaneous synaptic activation of SGNs persists in the absence of supporting cell Cx26. (a) Schematic of calcium imaging in SGNs in *Snap25-T2A-GCaMP6s* mice. (b) Temporally pseudocolored 50 s projection of coordinated spontaneous calcium transients in SGNs from isolated prehearing cochlea in control (*Gjb2*$^{fl/fl}$;*Snap25-T2A-GCaMP6s*, top) and Cx26 cKO (*Tecta-Cre;Gjb2*$^{fl/fl}$;*Snap25-T2A-GCaMP6s*, bottom). (c) Raster plot of $\Delta F/F_o$ signals from 30 randomly selected SGN ROIs in control (top) and Cx26 cKO (bottom) cochleae. Highlighted transients correspond by color to those indicated in b. (d) Quantification of spontaneous SGN calcium transient frequency, duration, and mean correlation coefficient. $N = 3$ control, 5 Cx26 cKO cochleae; $p = 0.7857$, 0.9345, 0.0114 (frequency, duration, and correlation), two-sample t test with Benjamini–Hochberg correction. (e) Raster plot of $\Delta F/F_o$ signals from 30 randomly selected SGN ROIs in a Cx26 cKO cochlea with addition of NBQX (50 μM). High potassium (High K^+) aCSF is added following NBQX to ensure intact calcium responses. (f) Quantification of calcium event frequency within Cx26 cKO SGNs with addition of NBQX. $N = 4$ Cx26 cKO cochleae; $p = 1.8187e\text{-}5$, paired t test. (g) (Left) Low magnification image of SGNs labeled by immunoreactivity to Tuj1 (cyan) in mid-modiolar cross section of P7 cochlea. Labels indicate locations of apical, middle, and basal SGN counts. (Right) Representative high-magnification images of SGN soma in apical, middle, and basal cochlea from control (*Gjb2*$^{fl/fl}$, top) and Cx26 cKO (*Tecta-Cre;Gjb2*$^{fl/fl}$, bottom) at P7. Dashed lines indicate SGN compartment used for area measurement. (h) Quantification of SGN density in apical, middle, and basal cochlea at P7. $N = 3$ control, 3 Cx26 cKO; $p = 0.5885$, linear mixed effects model. Analysis code, plotted figure panels, and statistical analysis can be found at: https://doi.org/10.5281/zenodo.7896212. aCSF, artificial cerebrospinal fluid; ROI, region of interest; SGN, spiral ganglion neuron.

https://doi.org/10.1371/journal.pbio.3002160.g004

S7c and S3 Video). Plots of event amplitude across both lobes of the IC revealed that spontaneous activity in both mouse lines was highly variable in both amplitude (Fig 5c, length of horizontal orange and blue lines) and left-right hemisphere dominance (Fig 5c, size of orange and blue circles), mirroring the stochastic nature of ATP release events in the cochlea. Overall,

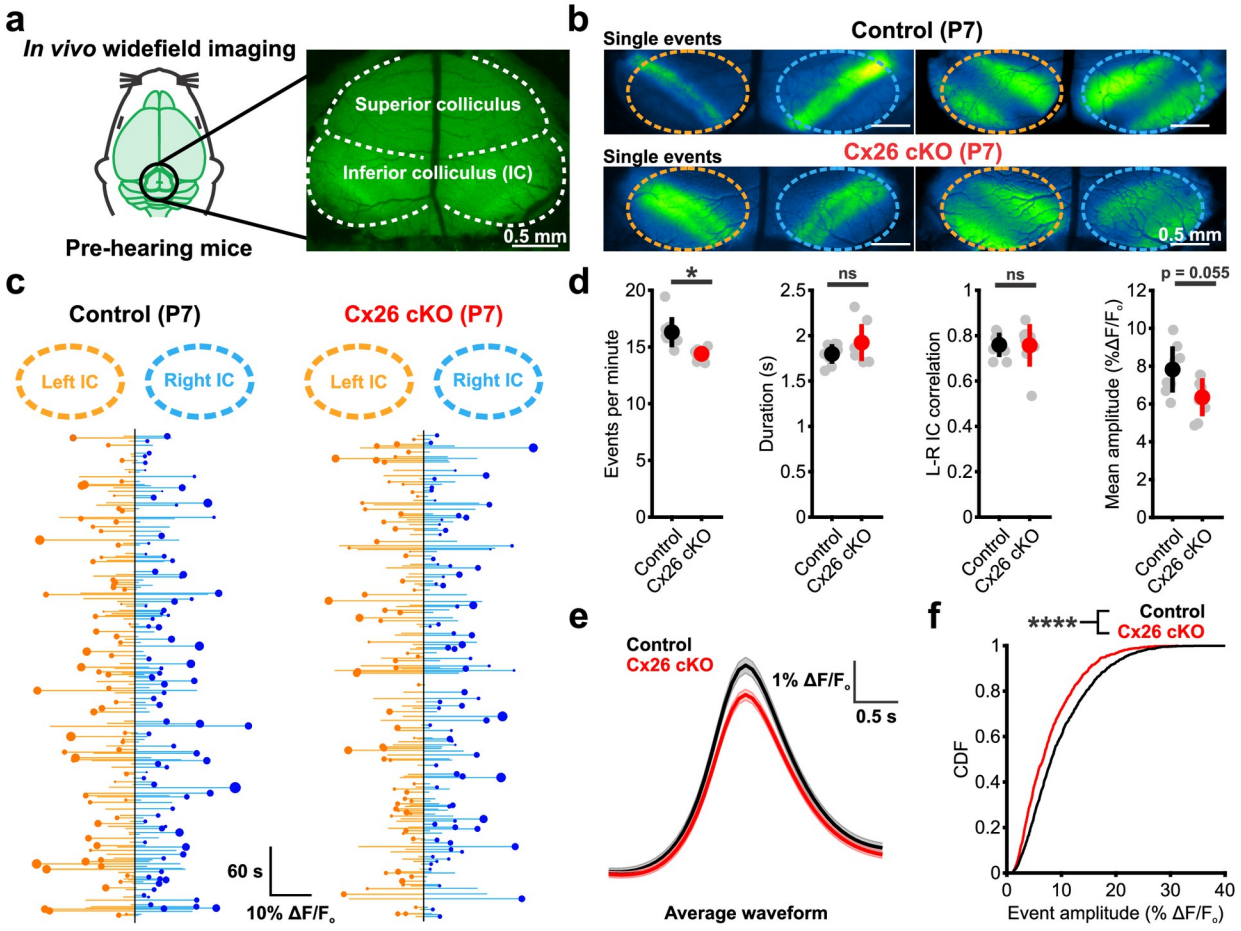

Fig 5. Spontaneous activity persists in the developing auditory system of Cx26 cKO mice. (a) Schematic of in vivo widefield epi-fluorescent imaging paradigm to visualize prehearing neural activity in the IC. (b) Representative single calcium events in P7 IC from control (*Gjb2*$^{fl/fl}$; *Snap25-T2A-GCaMP6s*, top) and Cx26 cKO (*Tecta-Cre;Gjb2*$^{fl/fl}$;*Snap25-T2A-GCaMP6s*, bottom) mice occurring within isofrequency bands along the future tonotopic axis of the IC. (c) Trace of spontaneous calcium transients over 10 min in the right and left inferior colliculi from control (left) and Cx26 cKO (right) mice. Each line represents a calcium event, circles indicate which colliculus (right vs. left) exhibited a larger amplitude during bilateral events, with the size of the circle indicating the relative difference in amplitude between right and left, with larger circles representing more asymmetric bilateral events. (d) Quantification of spontaneous calcium event frequency, duration, degree of correlation between right and left colliculi, and mean event amplitude. $n = 8$ control, 8 Cx26 cKO mice; $p = 0.0122, 0.2287, 0.9607, 0.0548$ (frequency, duration, correlation, and amplitude), two-sample t test with Benjamini–Hochberg correction. (e) Waveform of the mean spontaneous event aligned to peak amplitude from control and Cx26 cKO mice. $n = 1{,}315$ events from 8 control mice, 1,161 events from 8 Cx26 cKO mice. (f) Cumulative distribution plot of peak event amplitude. $n = 1{,}315$ events from 8 control mice, 1,161 events from 8 Cx26 cKO mice; $p = 2.8281\text{e-}11$, two-sample Kolmogorov–Smirnov test. Analysis code, plotted figure panels, and statistical analysis can be found at: https://doi.org/10.5281/zenodo.7896212. IC, inferior colliculus.

https://doi.org/10.1371/journal.pbio.3002160.g005

events were slightly less frequent and trended lower in mean amplitude in Cx26 cKO mice (Fig 5d); however, the bilateral nature and temporal kinetics (half-width) of these events were unchanged. Consistent with the trend towards smaller mean event amplitude, the average response peak was smaller and the cumulative distribution of event amplitudes and spatial integral were slightly shifted towards smaller events in Cx26 cKO mice, suggesting that fewer neurons were activated synchronously during each event (Figs 5e and 5f and S7d). While differences in the width of spontaneous events along the future tonotopic axis were not observed (S7e Fig), analysis of spontaneous events with two-photon imaging at single-cell resolution revealed subtle decreases in spatial activation of neurons in Cx26 cKO mice (S7f and S7g Fig)

consistent with observations in the isolated cochlea. Together, these in vivo results indicate that highly correlated bursts of neural activity continue to be induced in central auditory neurons prior to hearing, despite the lack of Cx26 expression within the organ of Corti.

Cx26 cKO mice exhibit reduced acoustic sensitivity but normal topographic organization

Despite the preservation of functional synaptic connections between IHCs and SGNs and robust spontaneous activity during early development in Cx26 cKO mice, these mice exhibited extreme auditory dysfunction by P21 (Fig 1). To determine if this functional deficit is present soon after hearing onset or develops later, we imaged sound-evoked neural activity within central auditory nuclei in unanesthetized mice just after ear canal opening (P13-P15) (Fig 6a), an approach that is more sensitive than ABRs, as detection does not require synchronous activation of large numbers of neurons and can be recorded without anesthesia. In control mice, unilateral sound stimuli (3 to 24 kHz sinusoidally amplitude-modulated pure tones) at a range of intensities (40 to 100 dB SPL) elicited neuronal activation within isofrequency domains of the IC (Fig 6b) [22]. Unexpectedly, stimulation with pure tones at >90 dB SPL also induced robust, tonotopically restricted activation of neurons within the IC of Cx26 cKO mice, allowing assessment of the functional organization of these regions. Plotting the evoked fluorescence profile along the tonotopic axis of the IC revealed that while the best frequency locations to suprathreshold, 100 dB SPL pure tone stimuli were slightly shifted along the tonotopic axis towards higher frequency (lateral) regions in Cx26 cKO mice (Figs 6c and S8a and S8b), proper spatial separation and normal width of isofrequency lamina were maintained (Figs 6d–6f and S8c). In accordance with ABR recordings at this age (S9a and S9b Fig), pure tone response thresholds were markedly elevated in Cx26 cKO mice relative to controls (Fig 6g and 6h); however, at suprathreshold sound intensities (>90 dB SPL), the average amplitudes and time courses of evoked calcium responses were comparable those recorded from control mice at 8 kHz and higher (Figs 6i and 6j and S8d and S8e). Notably, these elevations in auditory thresholds preceded substantial hair cell degeneration (S9c and S9d Fig), raising the possibility that structural alterations in the organ of Corti prevent proper amplification of sound-induced vibrations (S9e and S9f Fig).

To assess whether connections between the midbrain and thalamus enable transmission of sound evoked activity to the nascent auditory cortex (AC), we installed acute cranial windows over the AC and imaged sound-evoked responses without anesthesia just after ear canal opening (P13-P14, Fig 7a). In response to tones of different stimulus intensities, control mice exhibited several discrete foci of neuronal activity within primary (A1), suprarhinal (SRAF), and anterior (AAF) auditory cortical regions [52–54] (Fig 7b), consistent with the early establishment of tonotopic partitioning of acoustic information [55,56]. In response to loud tones, Cx26 cKO mice also exhibited sound-evoked neuronal activation with appropriate tonotopic organization that were comparable in amplitude to controls at similar sound intensities (Fig 7b and 7c); however, in accordance with decreased sensitivity observed in the IC, thresholds for neuronal responses in AC at these early ages were also much higher in Cx26 cKO mice (Fig 7d and 7e). Together, these results indicate that mice deprived of Cx26 in the organ of Corti retain proper tonotopic organization within auditory centers following ear canal opening, but exhibit a profound deficit in acoustic sensitivity.

Rapid increases in central gain after hearing onset in Cx26 cKO mice

Neural circuits within mouse central auditory centers adapt to the acoustic environment within a critical period in the third postnatal week [57–59]. We leveraged the increased

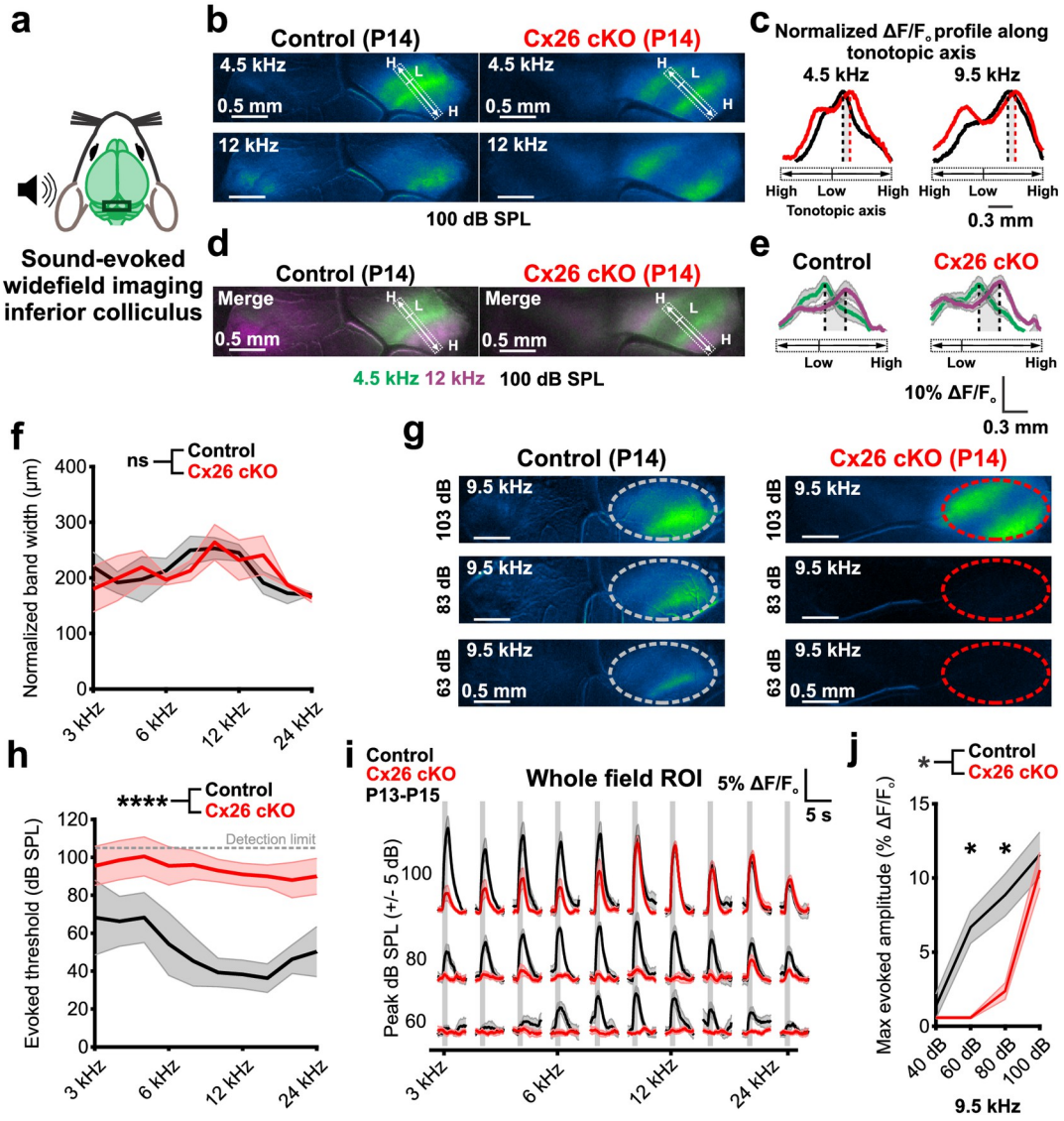

Fig 6. Reduced acoustic sensitivity but retained midbrain tonotopic organization in Cx26 cKO mice. (a) In vivo widefield imaging of tone-evoked IC neural activity in unanesthetized mice after hearing onset. (b) Suprathreshold tone-evoked neural calcium transients in IC from P14 control (*Gjb2*$^{fl/fl}$;*Snap25-T2A-GCaMP6s*, left) and P14 Cx26 cKO (*Tecta-Cre*;*Gjb2*$^{fl/fl}$;*Snap25-T2A-GCaMP6s*, right) mice. Rectangular ROIs were placed along the tonotopic axis of the contralateral IC (low (L) to high (H) frequency), perpendicular to pure tone evoked bands, to determine the peak response location for a pure tone. (c) Plot of tone-evoked normalized mean fluorescence along the tonotopic axis of the IC in control and Cx26 cKO mice. Dashed lines indicate location of peak pure tone response along tonotopic axis, gray shading indicates shift in peak response location for a given pure tone between control and Cx26 cKO mice. $n = 4$ control mice, 5 Cx26 cKO mice. (d) Pseudocolored tone-evoked calcium transients depicting spatial segregation of low and higher frequency stimuli along tonotopic axis. (e) Plot of tone-evoked mean fluorescence along the tonotopic axis of the IC in control (left) and Cx26 cKO (right) mice. Dashed lines indicate location of peak response along tonotopic axis, gray shading indicates spatial separation in peak response location for 4.5 (green) and 12 kHz (magenta) pure tones in control and Cx26 cKO mice. (f) Quantification of tone-evoked spatial activation (band width, 75th percentile) normalized to peak fluorescence response amplitude along the tonotopic axis of the IC at 100 dB SPL. $n = 4$ control, 5 Cx26 cKO mice; $p = 0.7575$, linear mixed effects model. (g) IC neural calcium transients to a 9.5 kHz stimulus from 103 to 63 dB SPL in a control and Cx26 cKO mouse. Circle in right IC depicts ROI for subsequent quantification of threshold and amplitude. (h) Quantification of tone-evoked thresholds. $n = 4$ control, 10 Cx26 cKO mice; $p = 1.6305e\text{-}6$, linear mixed effects model. (i) Quantification of tone-evoked fluorescence in IC across a range of frequency and sound level stimuli. Vertical gray bar indicates tone presentation. $n = 6$–7 control mice, 9–10 Cx26 cKO mice, mean ± SEM. (j) Rate-level functions characterizing maximum whole IC response amplitude at 9.5 kHz. Mean ± SEM, $n = 6$–7 control mice, 9–10 Cx26 cKO mice; $p = 0.0166$, linear mixed effects model with Sidák post hoc test. Analysis code, plotted figure panels, and statistical analysis can be found at: https://doi.org/10.5281/zenodo.7896212. IC, inferior colliculus; ROI, region of interest; SPL, sound pressure level.

https://doi.org/10.1371/journal.pbio.3002160.g006

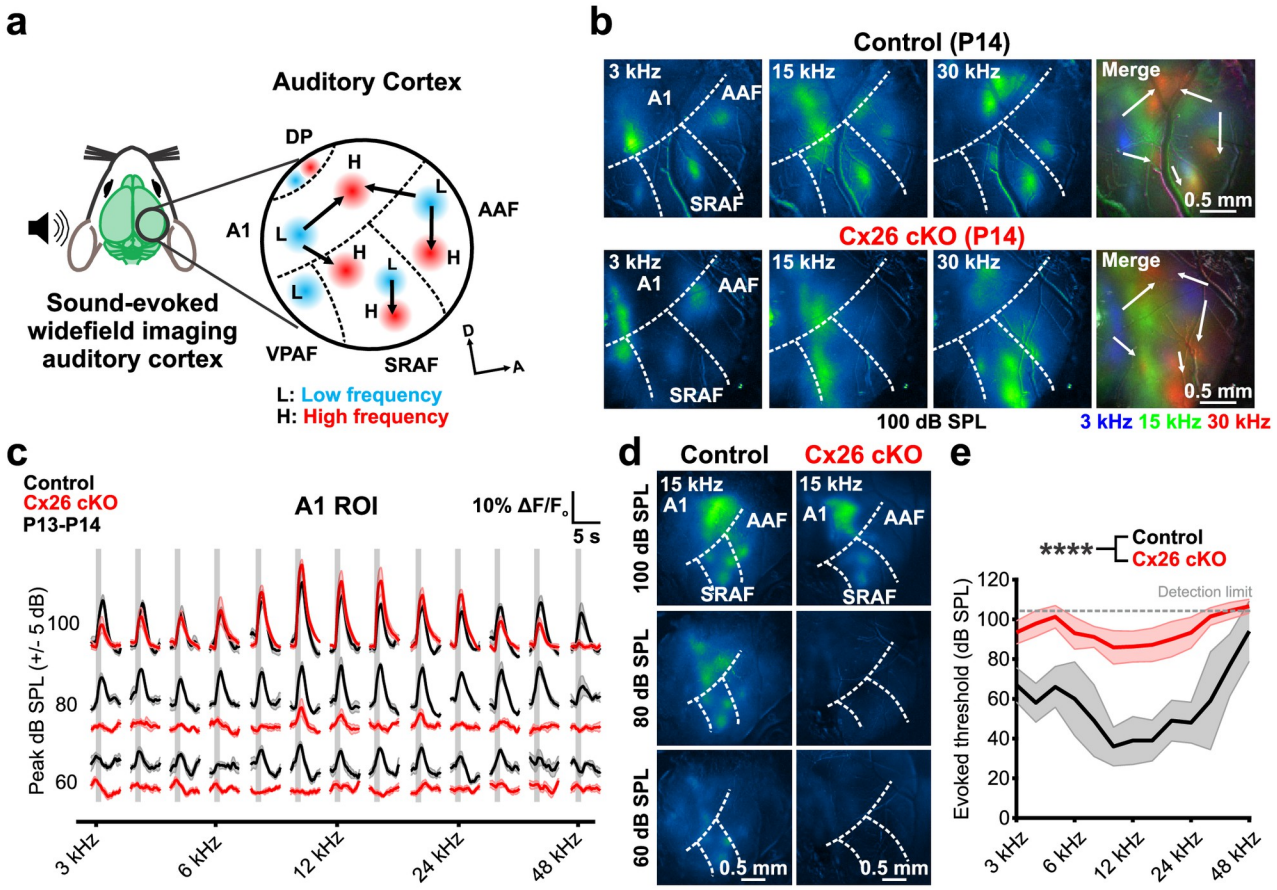

Fig 7. Suprathreshold stimuli elicit tonotopically organized calcium responses in auditory cortex of immature Cx26 cKO mice. (a) Schematic depicting tonotopic organization of mouse auditory cortex, adapted from [52,54]. L: low frequency, H: high frequency, A1: primary auditory cortex, AAF: anterior auditory field, SRAF: suprarhinal auditory field, VPAF: ventral posterior auditory field, DP: dorsal posterior. (b) Suprathreshold tone-evoked widefield neural calcium transients in AC from P14 control (*Gjb2*$^{fl/fl}$;*Snap25-T2A-GCaMP6s*) and P14 Cx26 cKO (*Tecta-Cre*;*Gjb2*$^{fl/fl}$;*Snap25-T2A-GCaMP6s*) mice. Merged image shows tonotopic segregation of pseudocolored pure tone responses from low (L) to high (H) frequency along tonotopic axes. (c) Quantification of tone-evoked fluorescence in A1 across a range of frequency and sound level stimuli in P13-P14 control and Cx26 cKO mice. Vertical gray bar indicates tone presentation. $n = 5$ control mice, 7 *Tmem16a* cKO mice, mean ± SEM. (d) AC neural calcium transients to a 15 kHz pure tone stimulus from 100 to 60 dB SPL in a control and Cx26 cKO mouse. (e) Quantification of tone-evoked thresholds. $n = 5$ control, 7 Cx26 cKO mice; $p = 8.8449e\text{-}6$, linear mixed effects model. Analysis code, plotted figure panels, and statistical analysis can be found at: https://doi.org/10.5281/zenodo.7896212. AC, auditory cortex; SPL, sound pressure level.

https://doi.org/10.1371/journal.pbio.3002160.g007

sensitivity of in vivo neuronal calcium imaging to assess how deprivation of normal acoustic input during this key developmental phase alters acoustic response characteristics. Similar to the responses in mice recorded just after hearing onset, pure tones at high intensity stimuli (80 to 100 dB SPL) elicited neuronal activation within auditory cortex of P21 Cx26 cKO mice (Fig 8a); however, while tone-evoked fluorescence amplitudes decreased between P14 and P21 in control mice, consistent with emerging local inhibition [55,60,61], Cx26 cKO mice exhibited an opposite trend, with evoked fluorescence amplitudes to suprathreshold stimuli increasing dramatically during this period (Fig 8a and 8b), resulting in steeper intensity-level functions than control mice and those observed in Cx26 cKO mice at P14 (Fig 8b and 8c). This increased fluorescence was accompanied by broader spatial activation to pure tones across auditory cortex, particularly within the mid-frequency range (Fig 8d and 8e), suggesting that more neurons may be responding to suprathreshold pure tones in Cx26 cKO mice. To characterize the cellular mechanisms underlying increased acoustic sensitivity in auditory

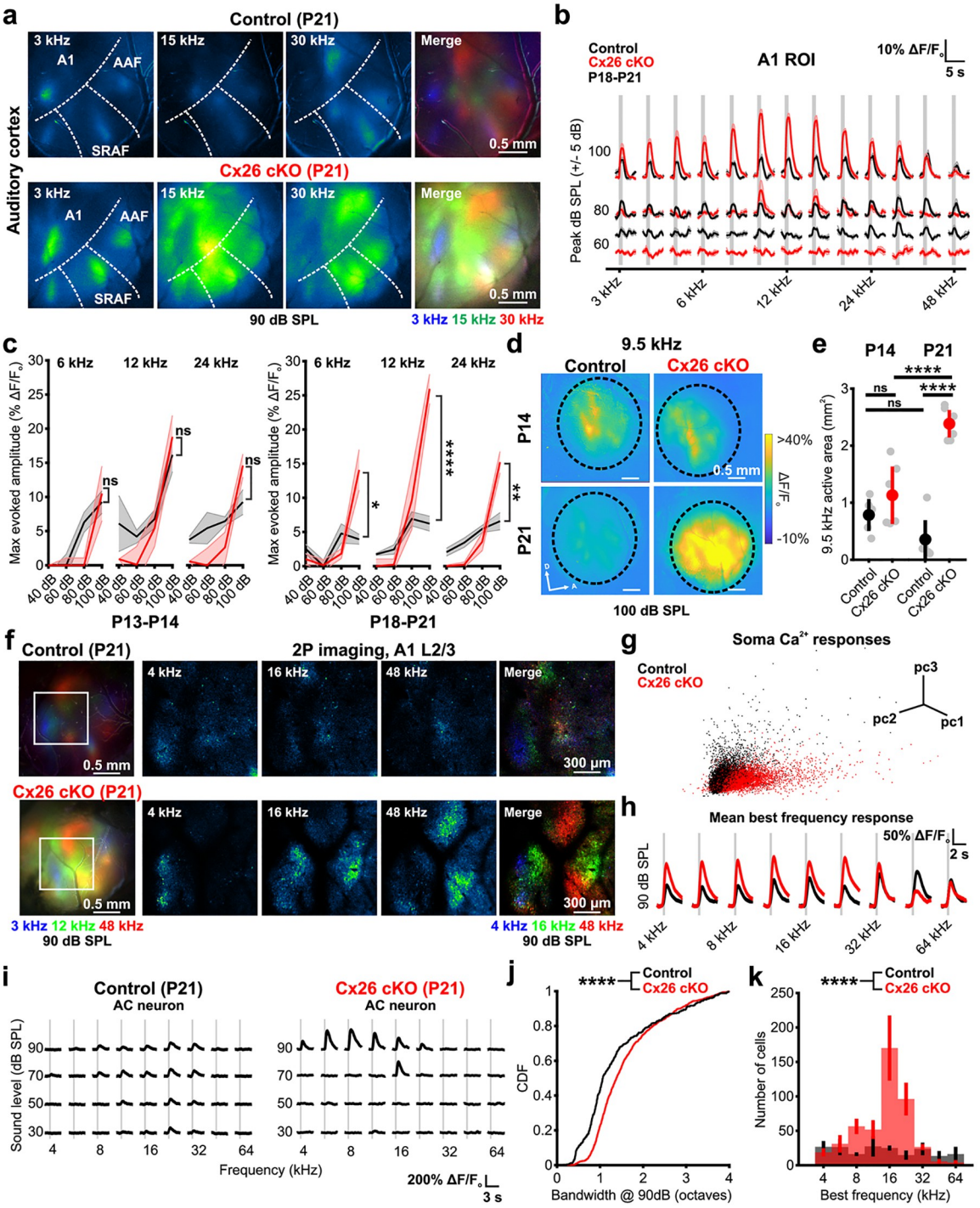

Fig 8. Rapid increases in central gain after hearing onset in Cx26 cKO mice. (a) Suprathreshold widefield neural calcium transients in AC from P21 control (*Gjb2*$^{fl/fl}$;*Snap25-T2A-GCaMP6s*) and P21 Cx26 cKO (*Tecta-Cre*;*Gjb2*$^{fl/fl}$;*Snap25-T2A-GCaMP6s*) mice. Merged image shows tonotopic segregation of pseudocolored pure tone responses along tonotopic axes. (b) Quantification of tone-evoked fluorescence in A1 across a range of frequency and sound level stimuli in P18-P21 control and Cx26 cKO mice. Vertical gray bar indicates tone presentation. $n = 7$ control mice, 9 *Tmem16a* cKO mice, mean ± SEM. (c) Rate-level functions characterizing maximum A1 response amplitude at 6, 12, and 24 kHz at P13-P14 (left) and P18-P21 (right). Mean ± SEM, $n = 7$ P18-P21, 5 P13-P14 control mice, 9 P18-P21, 7 P13-P14 Cx26 cKO mice; P13-P14: $p = 0.7551$, 0.5816, 0.2418, Wilcoxon rank sum test (6 kHz) or two-sample t test (12 kHz, 24 kHz) with Benjamini–Hochberg correction. P18-P21: $p = 0.0164$, 2.1097e-7, 0.0026, Wilcoxon rank sum test (6 kHz) or two-sample t test (12 kHz, 24 kHz) with Benjamini–Hochberg correction. (d) Normalized fluorescence responses in auditory cortex (circled) of control and Cx26 cKO mice at P14 and P21 to a 9.5 kHz pure tone stimulus at 100 dB SPL. (e) Quantification of activated area in

auditory cortex in response to a 9.5 kHz pure tone. n = 5 P13-P14, 6 P16-P21 control mice, 6 P13-P14, 7 P16-P21 Cx26 cKO mice; p = 5.8256e-8, one-way ANOVA with Tukey's HSD post hoc comparisons. (f) (Left) Widefield macroscopic tonotopic maps of auditory cortex in a P21 control (top) and Cx26 cKO (bottom) at 90 dB SPL. White square indicates A1 region for two-photon imaging. (Right) Neuronal tone-evoked fluorescence at 90 dB SPL in layer II/III of A1 from mouse at left. (g) Principal component analysis of maximum tone-evoked fluorescence to a range of frequency (4–64 kHz) and sound intensity (30–90 dB SPL) stimuli. Each dot represents fluorescence signals of a single neural soma. n = 3 control, 3 Cx26 cKO mice. (h) Mean tone-evoked fluorescence at 90 dB SPL of all neurons sorted by their best frequency stimulus. (i) Tone-evoked fluorescence in a representative A1 neuron to a range of frequency and intensity stimuli in a control and Cx26 cKO mouse. (j) Cumulative distribution of neural tone-evoked frequency bandwidth at 90 dB SPL as measured by a Gaussian fit of maximum evoked fluorescence. n = 432 control cells (3 mice), 1,088 Cx26 cKO cells (3 mice); p = 1.8327e-14, two-sample Kolmogorov–Smirnov test. (k) Histogram of mean number of tone-responsive neurons binned by their best frequency. n = 567 control cells (3 mice), 1,379 Cx26 cKO cells (3 mice); p = 7.3571e-15, two-sample Kolmogorov–Smirnov test. Analysis code, plotted figure panels, and statistical analysis can be found at: https://doi.org/10.5281/zenodo.7896212. AC, auditory cortex; SPL, sound pressure level.

https://doi.org/10.1371/journal.pbio.3002160.g008

cortex, we performed in vivo two-photon imaging of layer II/III in primary auditory cortex (A1) at P21 (Fig 8f). Individual cortical neurons from Cx26 cKO mice exhibited fluorescence response patterns distinct from control cells when presented with pure tone stimuli across multiple sound levels, revealed by principal component analysis clustering (Fig 8g), with larger fluorescence amplitudes to a given best frequency suprathreshold stimulus (Fig 8h). Broader spatial activation to suprathreshold pure tones in AC could result from a wider frequency sensitivity of individual AC neurons; however, we observed only a modest increase in the bandwidth of sharply tuned AC neurons in Cx26 cKO mice (Fig 8i and 8j). In contrast, there was a dramatic increase in the total number of AC neurons engaged by suprathreshold pure tones (9 frequencies, 4 to 64 kHz, 30 to 90 dB SPL) in Cx26 cKO mice (Total visualized neurons activated: control, 6.9 ± 2.7%; Cx26 cKO, 13.0 ± 4.4%) across a wider range of cortical territory, particularly for neurons tuned to mid-frequency stimuli (Fig 8k), providing an explanation for the broader activation and greater spatial synchrony of auditory neuron responses to acoustic input. Together, these results reveal that although developmental spontaneous neural activity is preserved in the absence of Cx26, cessation of this burst firing after ear canal opening and the resulting loss of ascending input results in rapid adaptation of auditory neurons, leading to enhanced gain, broader frequency tuning, and hypersynchrony of neurons within central auditory centers.

Discussion

Loss of function variants in *Gjb2* are a leading cause of inherited deafness worldwide, but the mechanisms responsible for these hearing deficits are unknown and there are no approved therapies to restore Cx26 function in these patients. Despite evidence of developmental changes in the structure of the organ of Corti and progressive hair cell degeneration [15], children with *Gjb2* variants respond better to cochlear implants following early implantation relative to other deafness etiologies [16,62,63], suggesting that their central auditory circuits can process acoustic information effectively. Our studies, which involve analysis of mice in which *Gjb2* was selectively inactivated within the cochlear sensory epithelium, reveal that intrinsically generated spontaneous activity that emerges from the developing cochlea prior to hearing onset persists in absence of these gap junctions, providing the means to promote neuronal survival, refine frequency tuning, and establish proper gain of auditory neurons during a critical developmental period [33]. Preservation of this spontaneous, correlated burst firing from the cochlea to the auditory CNS was unexpected, as cochlear supporting cells form a highly interconnected syncytium using Cx26 gap junctions, which coordinates their maturation and enables ion redistribution following mechanotransduction. Moreover, Cx26 hemichannels can serve as a conduit for the release of ATP [26], which initiates these periodic bursts of activity in

the cochlea prior to hearing onset. Nevertheless, ISCs in the developing cochlea remained highly coupled in the absence of Cx26 and retained the ability to release ATP in a spatially and temporally restricted manner, allowing coordinated excitation of groups of IHCs along the length of the cochlea. These studies highlight the unexpected resilience of both the pan-supporting cell syncytium in the organ of Corti and the mechanisms responsible for initiating spontaneous activity in the developing auditory system. Our studies also reveal that cessation of spontaneous activity and deficiencies in transmission of acoustic information at hearing onset led to a rapid, progressive increase in auditory neuron excitability, insight that may help improve the performance of cochlear implants in patients with variants in *Gjb2*.

Intercellular coupling and ATP release in the absence of Cx26

Gap junctions have been implicated in coordinating the development and physiological state of the cochlear sensory epithelium by allowing transfer of microRNAs and second messengers such as IP3 and calcium through the supporting cell syncytium [64–66]. This intercellular signaling is thought to be mediated primarily by Cx26 and Cx30, the most prevalent gap junction proteins expressed by supporting cells in both the developing and mature cochlea [6,67,68]. Over 50 distinct variants in *Gjb2* have been identified and studies in heterologous expression systems indicate that most result in loss of function due to impaired trafficking and assembly [10]. Moreover, genes encoding these proteins, *Gjb2* and *Gjb6*, respectively, are adjacent in the genome and their expression is co-regulated, with mutations in *Gjb2* lowering *Gjb6* transcription protein level and vice-versa [35,40,69], suggesting that disruption of *Gjb2* should substantially impair coupling and coordinated cellular signaling in the developing organ of Corti. Although tracer spread between ISCs was reduced, and ATP-dependent increases in calcium and resulting osmotic crenations were more spatially restricted in Cx26 cKO mice, supporting cells adjacent to IHCs (including future inner phalangeal cells) in Cx26 cKO mice retained gap junctional coupling sufficient to enable transfer of tracer and high electrical coupling. Previous studies have shown that Cx30 KO mice exhibit reduced spatial spread of spontaneous calcium transients [44], although the degree of intercellular coupling in Cx30 KO ISCs has not been assessed. It is not yet known which gap junctions enable this preservation of coupling in Cx26 cKO mice or whether it arises through retained expression or compensatory up-regulation of latent gap junctions. Recent single-cell sequencing of the developing sensory epithelium suggests that additional gap junctions are expressed within Kölliker's organ at this age, including *Gja1* (Cx43) and *Gjc1* (Cx45) [70–72], albeit at substantially lower levels compared to *Gjb2* or *Gjb6*. Although ISCs remained coupled in the absence of Cx26, developmental abnormalities in the structure of the cochlear epithelium remained, including agenesis of the tunnel of Corti and Nuel's space, demonstrating a distinct requirement for Cx26 beyond ISC intercellular coupling.

Connexin hemichannels (unpaired connexin channels in the plasma membrane) can allow ATP release [26,73], raising the possibility that they may enable activation of P2RY1 autoreceptors on ISCs [32,42]. Despite the high expression of Cx26 in ISCs, spontaneous ATP release events persist in both Cx26 cKO and Cx30 KO mice [44,74], indicating that Cx26 (and Cx30) hemichannels are not essential conduits for ATP release in the developing cochlea. Although pannexin channels and purinergic P2rx7 channels can also mediate ATP release and Pannexin 1 is expressed by ISCs [70], spontaneous calcium transients persist in ISCs of prehearing cochlea in the absence of Pannexin 1 [75] or P2rx7 [76] channels. It is plausible that remaining gap junction hemichannels or other anion channels enable ATP release from these cells. The low frequency of these events suggest that spontaneous activity could be supported by only a few channels per cell, if their gating probability and ATP permeability were sufficiently high.

Early establishment of tonotopic organization and cortical gain in deaf mice

Cx26 cKO mice exhibited profound auditory dysfunction following ear canal opening, with elevated ABR thresholds and reduced activation of neurons in the IC and AC as early as P13. Nevertheless, ABRs and sound-evoked neural calcium increases in the IC and AC could still be elicited with suprathreshold (>80 to 90 dB SPL) pure tone stimuli at these early ages, indicating that cochlear mechanotransduction and signal propagation through auditory circuits still occurs. Recent studies indicate that prehearing spontaneous burst firing is required to establish proper gain and frequency tuning of central auditory neurons, as well as consolidate sound processing domains within the brain [33,77]. Although Cx26 cKO mice were less sensitive to airborne sound, evoked calcium responses in IC and AC mirrored the amplitudes, spatial activation, and tonotopic organization of neuronal activity of control mice, suggesting that the persistence of prehearing spontaneous activity promoted restricted IHC activation along the sensory epithelium and refinement of auditory neuron projections during the prehearing period. These studies also indicate that alterations in cochlear structure and abnormal physiological maturation of IHCs in Cx26 or Cx30 [11,74] deficient mice do not prevent IHC burst firing or propagation of tonotopically restricted spontaneous events to the CNS needed to promote aspects of circuit maturation. Targeted deletion of Cx26 within the cochlea may not completely model central circuit development; however, as individuals with loss of function variants likely experience aberrant Cx26 expression throughout the CNS, with unknown effects on neuronal circuitry.

Despite preservation of normative patterns of neural activity prior to ear canal opening, auditory circuits in Cx26 cKO mice rapidly changed after this intrinsically induced activity ceased and IHC activation became dependent on airborne sound. The high threshold of sensory transduction within the cochlea of Cx26 cKO mice and corresponding decline in activity propagating through central auditory circuits was accompanied by enhanced gain to suprathreshold pure tones in auditory cortex. Moreover, Cx26 cKO mice at P21 exhibited extensive cortical activation to suprathreshold pure tone stimuli, with blurring of precise tonotopic domains, due to increased numbers of cortical neurons responding simultaneously with larger fluorescence amplitudes. Prior studies have shown that neurons in auditory cortex increase their excitability after hearing loss [78–81], which is associated with elevated non-evoked cortical activity and enhanced neural synchrony to residual stimulation that often overshoot beyond baseline levels [82–85]. Our results indicate that these changes in cortical circuits also occur following congenital hearing loss and that hypersynchrony to residual stimuli emerges primarily as a result of engagement of normally latent cortical neurons, presumably in part due to decreased inhibition [78,79,86,87]. Although attempting to compensate for reduced peripheral input, this increased central gain could prove detrimental and contribute to suprathreshold hyperacusis (disordered loudness perception) and tinnitus (perception of sound in absence of an acoustic stimulus) [88–91]. While the precise mechanisms underlying the emergence of tinnitus remain unclear and are likely multifactorial [90,92,93], cochlear implants have been shown to reduce tinnitus in individuals with severe hearing loss, suggesting that restoration of peripheral input may reverse these homeostatic changes [94,95] and that early intervention to restore hearing may improve functional outcomes in forms of congenital deafness arising from variants in *Gjb2*.

Mechanisms of peripheral auditory dysfunction due to loss of Cx26

The reduction in acoustic sensitivity observed in Cx26 cKO mice resembles that of cochlear-wide Cx26 deletion [12,35,36], including elevation of ABR thresholds (>50 dB

SPL), loss of DPOAEs, and progressive degeneration of hair cells. However, hair cell degeneration was delayed in Cx26 cKO mice relative to other models [12,35], allowing assessment of acoustic sensitivity prior to hair cell loss. Remarkably, deficiencies in sound detection manifested in Cx26 cKO mice prior to hair cell degeneration. Several other factors could contribute to this early auditory dysfunction, including aberrant IHC physiological maturation, structural abnormalities in the organ of Corti, and impaired endocochlear potential (EP) generation. Previous studies in other mouse models have shown that IHC membrane properties in both Cx26 and Cx30 KO mice do not mature properly, with aberrant resting membrane potential and potassium current expression, persistent SK2 channels, impaired synaptic release, and retained olivocochlear synaptic input by P16-P25 [74]. Structurally, Cx26 cKO mice failed to form the tunnel of Corti and Nuel's space in the organ of Corti [11,36], perhaps due to abnormal maturation of pillar cells and Deiters' cells. This structural disruption could impair cochlear amplification by preventing efficient coupling of OHC electromotility to the basilar membrane, leading to loss of DPOAEs and elevated ABR thresholds, as observed following OHC degeneration, supporting cell ablation, or compromised electromotility [96,97]. However, disruption of gap junction coupling specifically within pillar and Deiters' cells did not affect formation of the tunnel of Corti or Nuel's space, and reduced DPOAE sensitivity was only observed within basal cochlear regions [98,99], although these studies were not designed to assess an early developmental requirement for Cx26 expression and may have been hampered by incomplete *Gjb2* inactivation in *Prox1-CreER* mice [97,100].

EP reductions of 50% to 70% have been observed in models of both cochlea-wide and organ of Corti restricted deletion of Cx26 [11,35], which could also impair hair cell mechanotransduction and cochlear amplification. However, mice that express a dominant negative variant of Cx26 (R75W) exhibit auditory dysfunction, hair cell degeneration, and collapse of the tunnel of Corti and perilymphatic spaces, but retain a normal EP [101], suggesting that structural changes within the sensory epithelium may be sufficient to impair auditory sensitivity. As spontaneous neural burst firing in the prehearing cochlea does not require EP generation or OHC function and cochlear amplification, these impairments only manifest when spontaneous bursts of activity in the auditory nerve cease after ear canal opening. This mechanistic independence of intrinsically generated and sound-induced activities may enable preservation of early patterned activity in the developing auditory system in individuals that will later present with profound hearing impairment.

Materials and methods

Ethics statement

All experiments and procedures were approved by the Johns Hopkins Institutional Care and Use Committee (Protocol #M018M330, #M021M290).

Animals

This study was performed in strict accordance with the recommendations provided in the Guide for the Care and Use of Laboratory Animals of the National Institutes of Health. Generation and genotyping of transgenic mice, including *Cx26*$^{fl/fl}$ (European Mouse Mutant Archive EM:00245) [11], *Tecta-Cre* (JAX Stock No. 035552) [32], *R26-lsl-GCaMP3* [45], *R26-lsl-eGFP* (MMRRC Stock No. 32037-JAX) [102], and *Snap25-T2A-GCaMP6s* (JAX Stock No. 025111) [47] have been previously described. All animals were backcrossed and maintained on a C57Bl/6N background. Both male and female mice were used for all experiments.

Cochlea histology and immunohistochemistry

Mice were deeply anesthetized with inhaled isoflurane (<P14) or intraperitoneal injection of 10 mg/ml sodium pentobarbital (>P14) and cardiac perfused with ice cold 1× PBS followed by 4% paraformaldehyde (PFA) in 0.1 M phosphate buffer (pH 7.4). The inner ear was isolated from the temporal bone, post-fixed in 4% PFA overnight at 4˚C and stored in 1× PBS with 0.1% sodium azide until processing. For cross sections, cochleae were decalcified in 10% EDTA in 0.1 M phosphate buffer (pH 7.4) shaking at 4˚C (P7: 2 to 4 h, >P14: 48 h), cryopreserved in 30% sucrose, embedded in O.C.T. compound (Tissue Tek), cut in 10 μm sections using a cryostat, and placed on slides (SuperFrost Plus, Fisher). Cochlea sections and free-floating whole cochlea were preincubated in blocking solution (0.3% to 0.5% Triton X-100, 5% Normal Donkey Serum in PBS (pH 7.4)), and incubated at 4˚C with primary antibodies (Mouse anti-Cx26, 1:100, Invitrogen; Rabbit anti-Cx26; 1:250, Invitrogen; Rabbit anti-Cx30, 1:250, Invitrogen; Rabbit anti-MyosinVIIa, 1:300, Proteus Biosciences; Goat anti-Calbindin, 1:200, Santa Cruz, Rabbit anti-β3-tubulin, 1:500, Cell Signaling Technologies). Following overnight incubation, cochleae were washed 3 × 10 min in PBS and incubated with corresponding donkey secondary antibodies (Alexa Fluor 488, Alexa Fluor 546, and Alexa Fluor 647; 1:2,000, Invitrogen) for 2 h at room temperature. For assessment of Neurobiotin spread, cochleae were incubated with conjugated Alexa Fluor 555-Streptavidin (1:1,000) for 2 h during secondary antibody incubation. Finally, slides were washed, incubated with 1:10,000 DAPI, and sealed using Aqua Polymount (Polysciences). For hematoxylin and eosin staining, cochleae were decalcified, dehydrated in 70% ethanol, embedded in paraffin, cut in 5 μm sections, and stained by the Reference Histology core in the Department of Pathology at Johns Hopkins Hospital. Images were captured using an epifluorescence microscope (Keyence BZ-X) or a laser scanning confocal microscope (LSM 880, Zeiss).

Quantification of hair cells and spiral ganglion neurons

For analysis of hair cell density, decalcified cochleae were dissected and cut into 3 segments of equal length (apex, middle, and base) and stained for hair cell markers as described above. Images of MyoVIIa immunoreactivity were collected at 25× magnification at the mid-portions of each segment corresponding roughly to 8 kHz, 24 kHz, and 50 kHz, respectively. Quantification of cell density was performed in a blinded fashion using a custom cell counting algorithm (MATLAB), described below, or manually, when restricted by low signal-to-noise. For automated counts and analysis of degenerating OHCs, maximum intensity projections of hair cells were thresholded and binarized, a mask placed over the OHC region, and counts of "preserved" OHC centroids were identified using the MATLAB function "bwboundaries."

For analysis of SGNs, 10-μm thick mid-modiolar cross sections were identified, and images collected from the apical, middle, and basal spiral ganglia visible within that section. SGN density was determined in a blinded manner by first measuring the spiral ganglion area in ImageJ and subsequent manual counts of all visible Tuj1-labeled neuronal soma. If multiple mid-modiolar sections were visualized on the same slide, images were collected from all regions and averaged.

Auditory brainstem response (abr) and distortion product otoacoustic emission (dpoae) measurements

For both ABR and DPOAE measurements, mice were anesthetized by intraperitoneal injection of ketamine (100 mg/kg) and xylazine (20 mg/kg) and placed in a sound attenuation chamber.

Body temperature was maintained at 37˚C using a rectal temperature probe and feedback heating pad (ABRs) or an isothermal heating pad (DPOAEs).

For ABR assessment, subdermal platinum needle electrodes (E2, Grass Technologies) were placed posterior to the pinna, at the vertex, and leg (ground). Stimuli and signal acquisition were controlled using a custom MATLAB program [103]. Acoustic stimuli consisted of 1 ms clicks and 5 ms tone pips of varying frequency (8, 16, 24, and 32 kHz) at a rate of 20 Hz. Signals were generated by a TDT System 3 (Tucker Davis Technologies), amplified (Crown CH1, Crown Audio), and delivered through a free-field speaker (FD28D, Fostex) placed 30 cm away from the pinna with 5 to 10 dB attenuation steps. The speaker was calibrated with a free-field microphone (type 4939, Brüel & Kjær) at 30 cm. ABR signals were amplified (Iso-80, World Precision Instruments) band-pass filtered (Krohn-Hite Model 3550, Krohn-Hite Corporation), digitized (RX6 Multifunction Processor, Tucker Davis Technologies), and averaged across 300 stimuli. ABR thresholds were calculated in an automated manner as the lowest stimulus intensity determined by linear interpolation that produced peak-to-peak ABR signals that were greater than 2 standard deviations above the peak-to-peak background signal. Average ABR traces represent mean +/− standard deviation (shaded region) across all animals.

For DPOAE assessment, an ER10B+ microphone probe (Etymotic Research) with a 3 mm eartip (Etymotic Research 10D-T03) was securely placed in the external ear canal. Continuous pure tones (F1 and F2) were generated by an RZ6 Processor (Tucker Davis Technologies) and presented using 2 closed-field MF1 speakers (Tucker Davis Technologies) connected to the microphone probe by 3 cm of 1/8" PVC tubing. Tones were based at 5 center frequencies (Fc: 8, 12, 16, 20, and 24 kHz) with F1 = 0.909*Fc and F2 = 1.09*Fc. Primary tones were presented in 5 dB attenuation steps from 90 dB SPL to 20 dB SPL. Recording was performed at 20 ms intervals, and responses were averaged 300 times per attenuation level. Tone presentation and recording was controlled by BioSigRZ software (Tucker Davis Technologies). All DPOAEs were recorded blinded to animal genotype. DPOAE thresholds were calculated in an automated manner in MATLAB as the lowest stimulus intensity determined by linear interpolation that produced a peak at the expected DPOAE location (2F1-F2) that were greater than 2 standard deviations above the mean background signal adjacent to that frequency location. Average DPOAE traces represent mean +/− standard deviation (shaded region) across all animals of a given genotype.

Electrophysiology

Apical segments of the cochlea were acutely isolated from P6-P8 mouse pups and used within 2.5 h. Cochlea were dissected and subsequently superfused by gravity at 2 ml/minute with bicarbonate-buffered artificial cerebrospinal fluid (aCSF) at room temperature (22 to 24˚C) containing (in mM): 115 NaCl, 6 KCl, 1.3 $MgCl_2$, 1.3 $CaCl_2$, 1 NaH_2PO_4, 26.2 $NaHCO_3$, 11 D-glucose saturated with 95% O_2/5% CO_2 at a pH of 7.4. Whole cell recordings from ISCs were made under visual guidance using differential interference contrast transmitted light. Electrodes had tip resistances between 2.5 and 4.0 MΩ with internal solution of (in mM): 134 KCh_3SO_3, 20 HEPES, 10 EGTA, 1 $MgCl_2$, 0.2 Na-GTP, pH 7.4. Measurements of membrane resistance in ISCs were obtained following break in through 10 mV voltage steps from −20 to +20 mV relative to the holding potential. Spontaneous currents were recorded with ISCs held at −80 mV for a minimum of 10 min. For cell filling experiments, Neurobiotin (Vector Laboratories) was included in the internal solution at a final concentration of 0.2%. Recordings with Neurobiotin in the patch pipette were not included in analysis of spontaneous activity or input resistance, but did not exhibit any significant differences from recordings without Neurobiotin. For recordings from IHCs, electrodes had tip resistances between 4.0 and 6.0 MΩ with

internal solution of (in mM) 134 KCh_3SO_3, 20 HEPES, 10 EGTA, 1 $MgCl_2$, 0.2 NaCl, pH 7.4. Resting potential measurements were made immediately following cell membrane rupture in current clamp configuration with no current injection. Measurements of membrane resistance in IHCs were obtained through repeated 10 mV voltage steps from −10 to +10 mV relative to the holding potential, and I-V curves were generated through 10 mV voltage steps from −150 to +20 mV. Spontaneous currents were recorded with IHCs held at −70 mV for a minimum of 15 min. Recordings were performed using pClamp 9 software with a Multiclamp 700A amplifier (Axon Instruments), low pass Bessel filtered at 1 kHz, and digitized at 5 kHz (Digidata 1322a, Axon Instruments). Recordings exhibiting >20% change in access resistance or with access resistance >30 MΩ at the start of recording were discarded. Errors due to voltage drop across the series resistance and liquid junctional potential were left uncompensated. Application of MRS2500 (Tocris, 1 μM) was performed by superfusion by gravity of MRS2500-containing aCSF without interruption of continuous aCSF flow. Analysis of input resistance, resting membrane potential, and spontaneous activity was performed offline in MATLAB. Spontaneous currents were detected using the "peakfinder" function, with a fixed peak threshold (baseline + 3 standard deviations) and minimum peak amplitude (10 pA for ISCs, 5 pA for IHCs). Analysis of changes in spontaneous activity with MRS2500 was performed 1.5 min after change in perfusion, to allow time for inflow of drug into the bath.

Transmitted light imaging

For time-lapse imaging of spontaneous osmotic crenations, acutely excised cochleae were visualized using DIC optics through a 40× water-immersion objective coupled to a 1.8× adjustable zoom lens (Zeiss) on a Zeiss Axioskop 2 microscope. Images were acquired at 1 frame per second using a frame grabber (LG-3; Scion) and Scion Image software. Crenations were detected by generation of difference movies in Matlab through subtraction of frames at time t_n and t_{n+5} seconds. To detect transmittance change events, a threshold of the mean + 3 standard deviation was applied to the difference signal. To calculate area of crenation events, a Gaussian filter (sigma = 12) was applied to the image after thresholding and the borders detected using MATLAB ("bwlabel" function). The crenation area was calculated as the number of pixels within the border multiplied by a scaling factor $(\mu m/pixel)^2$.

Cochlea explant culture and calcium imaging

Cochlea segments were acutely isolated from P5-P6 mice in ice-cold, sterile filtered, HEPES-buffered aCSF containing (in mM): 130 NaCl, 2.5 KCl, 10 HEPES, 1 NaH_2PO_4, 1.3 $MgCl_2$, 2.5 $CaCl_2$, 11 D-glucose, as previously described [22,46]. Explants were mounted onto Cell-Tak (Corning) treated coverslips and incubated at 37˚C for 12 h in Dulbecco's modified Eagle's medium (F-12/DMEM; Invitrogen) supplemented with 1% fetal bovine serum (FBS) and 10 U/ml penicillin (Sigma) prior to imaging. After overnight culture, cochleae were transferred to recording chamber and superfused with bicarbonate-buffered aCSF containing (in mM): 115 NaCl, 6 KCl, 1.3 $MgCl_2$, 1.3 $CaCl_2$, 1 NaH_2PO_4, 26.2 $NaHCO_3$, 11 D-glucose saturated with 95% O_2/5% CO_2 at a pH of 7.4 at room temperature (22 to 24˚C). For IHC and ISC imaging, cochleae were illuminated with a 488 nm laser (maximum 25 mW power), and optical sections containing both IHCs and ISCs were obtained with a pinhole set to 3.67 Airy units, corresponding to 5.4 μm of z-depth. For SGN imaging, the pinhole was set to 2.42 Airy units, corresponding to 3.6 μm of z-depth. Addition of NBQX disodium salt (Tocris, 50 μm) in aCSF and high-potassium aCSF (containing (in mM): 80 NaCl, 40 KCl, 1.3 $MgCl_2$, 1.3 $CaCl_2$, 1 NaH_2PO_4, 26.2 $NaHCO_3$, 11 D-glucose saturated with 95% O_2/5% CO_2 at a pH of 7.4) was performed through superfusion by gravity without interruption of continuous aCSF flow.

Images were captured at 2 Hz using a Zeiss laser scanning confocal microscope (LSM 710, Zeiss) through a 20× objective (Plan APOCHROMAT 20×/1.0 NA) at 512 × 512 pixels (425.1 by 425.1 microns).

Analysis of in vitro calcium imaging

All image analysis was performed in MATLAB. To assess spontaneous calcium activity within ISCs, a grid of 10 × 10 pixel squares were overlaid on the ISC region, as previously described [42]. Images were normalized to the 10th percentile for each pixel (F_o), and fluorescence changes ($\Delta F/F_o$, where $\Delta F = F–F_o$) were calculated for each region of interest (ROI) over the course of the 10-min movie. Each grid was binarized as active when $\Delta F/F_o$ was greater than median + 3 standard deviations of the $\Delta F/F_o$ signal. ISC events were defined by contiguous activation of connected ISC ROIs in 3 dimensions, with removal of events lasting fewer than 3 frames or less than 5 connected ROIs. Temporally and spatially overlapping events were separated by k-means clustering and visually confirmed as distinct calcium transients.

To assess spontaneous calcium activity within IHCs, oval ROIs aligned with the axis of the cell body were placed over each IHC soma within the field of view, with careful exclusion of phalangeal cell processes, and pixels within each ROI were averaged. Fluorescence changes with time were normalized as $\Delta F/F_o$ values, where F_o was the median fluorescence intensity during the 10-min recording period for each ROI. Signal peaks were detected ("findpeaks" function) with fixed peak threshold criteria (median + 3 standard deviations of $\Delta F/F_o$ signal) and minimum peak amplitude (10% $\Delta F/F_o$). To determine the number of IHCs activated during a given ISC calcium transient, the number of IHCs with event peaks between the start and end time of each ISC calcium event was counted. If temporal windows for ISC events overlapped, IHCs were assigned to the first ISC event in which they are activated, and not counted in subsequent overlapping events. To generate correlation matrices, pairwise Pearson's correlation coefficients were determined between every possible IHC pair. Mean correlation coefficients were defined as the average of the 80th percentile correlation coefficient between IHCs in the cochlea prep.

To assess spontaneous activity within SGNs, circular ROIs were drawn around each SGN soma on a maximum projection image. Fluorescence changes with time were normalized as $\Delta F/F_o$ values, where F_o was the median fluorescence intensity during the 10-min recording period for each ROI. Signal peaks were detected ("findpeaks" function) with fixed peak threshold criteria (median + 3 standard deviations of $\Delta F/F_o$ signal) and minimum peak amplitude (10% $\Delta F/F_o$). Only neurons that exhibited a $\Delta F/F_o$ response greater than 10% to 40 mM K^+ wash were included for analysis. Analysis of changes in spontaneous activity with NBQX was performed 1.5 min after change in perfusion, to allow time for inflow of drug into the bath.

In vivo imaging of spontaneous activity

Installation of early neonatal cranial windows has been previously described [22]. Briefly, mice were anesthetized in inhaled isoflurane (4% induction, 1.5% maintenance), the dorsal skull exposed to allow for headbar implantation, and a cranial window placed over the resected intraparietal bone overlying the midbrain or over auditory cortex (3.5 mm lateral to lambda), as previously described. In a subset of experiments, aCSF containing sulfarhodamine 101 (SR101, 10 μm) was washed over the brain surface before sealing of the cranial window to label astrocytes to enable image registration and motion correction. After 1 h of postsurgical recovery from anesthesia, neonatal mice were moved into a 15 ml conical tube (to swaddle and limit movement) and head fixed under the imaging microscope. During imaging, pups were maintained at 37˚C using a heating pad and temperature controller (TC-1000; CWE). Widefield

epifluorescence images were captured at 10 Hz using a Hamamatsu ORCA-Flash4.0 LT digital CMOS camera attached to a Zeiss Axio Zoom.V16 stereo zoom microscope illuminated continuously with a metal halide lamp (Zeiss Illuminator HXP 200C). Each recording of spontaneous activity consisted of uninterrupted acquisition over 10 min. Two-photon imaging was performed using a Zeiss 710 LSM microscope with two-photon excitation achieved by a Ti: sapphire laser (Chameleon Ultra II; Coherent) tuned to 920 nm. Images were collected at 4 Hz (256 × 256 pixels, 425 × 425 μm) from 150 μm Z-depth in the central IC for a minimum of 10 min.

For widefield imaging analysis, images were imported into MATLAB, underwent photobleaching correction by fitting a single exponential to the fluorescence decay and subtracting this component from the signal, and intensities were normalized as $\Delta F/F_o$ values, where $\Delta F = F–F_o$ and F_o was defined as the 10th percentile value for each pixel. Oval regions of interest were placed over the right and left IC, and signal peaks were identified using built-in peak detection ("findpeaks") with a fixed threshold (1% $\Delta F/F_o$) and minimum peak amplitude (1% $\Delta F/F_o$). Occasional spontaneous broad activation of the cortex and SC would elicit fluorescence increases in the IC, and these events were not included in the analysis, as they do not appear to be derived from the auditory periphery [22]. For analysis of spatial band width, a 25 × 100 rectangular ROI rotated 45 to 55 degrees was placed over each IC aligned with the future tonotopic axis of the IC. The rectangle was averaged along the short axis, creating a 100 × 1 pixel line scan of the tonotopic axis of the IC for the duration of the time series. Events were detected using the function "imregionmax" with a fixed threshold (2% $\Delta F/F_o$). The spatial integral of spontaneous events along the tonotopic axis was estimated using the function "trapz." Line scans of individual events were normalized to the maximum $\Delta F/F_o$ at that time point, and the band width calculated as the length along the tonotopic axis above the 75th percentile of the peak $\Delta F/F_o$. Two-photon imaging analysis was performed similarly, with a 50 × 300 pixel rectangular ROI rotated 45 to 55 degrees was placed over the imaging plane to be perpendicular to spontaneous bands. The rectangle was averaged along the short axis, creating a 300 × 1 pixel line scan of the tonotopic axis of the IC for the duration of the time series. Events were detected using the function "imregionmax" with a fixed threshold (2% $\Delta F/F_o$). Line scans of individual detected events were normalized to the maximum $\Delta F/F_o$ at that time point, and the band width calculated as the length along the tonotopic axis above the 75th percentile of the peak $\Delta F/F_o$.

Sound-evoked calcium imaging

Cranial windows over IC in P13-P15 mice were performed as previously described for P7 animals, with animals allowed to recover a minimum of 2 h prior to imaging. Auditory cortex windows in P13-P21 mice were installed using a microblade and microscissors to remove an approximately 4 mm circular region of skull overlying the right auditory cortex. Following skull removal, the dura was carefully removed using microscissors and exposed brain was continuously immersed in aCSF. A 5 mm coverslip was attached using superglue, and animals were allowed to recover a minimum of 2 h prior to imaging. During imaging, awake animals were head fixed but on a freely-rotating tennis ball to simulate natural movement.

Acoustic stimuli for widefield imaging were presented using a free-field speaker (MF1; Tucker Davis Technologies) placed 10 cm from the left ear within a custom sound attenuation chamber with external noise attenuation of 40 dB [22]. Stimuli consisted of 4 to 6 repetitions of sinusoidal amplitude modulated pure tones (1 s, 10 Hz modulation) from 3 to 48 kHz in ¼ octave intervals. All stimuli were cosine-squared gated (5 ms) and played in a random order at 5 s intervals. Tones were generated within the RpvdsEx software (Tucker Davis Technologies),

triggered using the microscope's frame out signal, and delivered through the RZ6 Audio Processor (Tucker-Davis Technologies). Calibration of the free-field speaker was performed using an ACO Pacific microphone (7017) and preamplifier (4016). Given the flat intensity profile (peak 100 dB SPL +/− 5 dB for a 2.0 V stimulus across all tested frequencies), levels were not corrected across presented frequencies. Stimuli were presented from 100 dB to 20 dB SPL in 10 to 20 dB attenuation steps.

For sound-evoked two-photon imaging, auditory cortex was first identified using widefield imaging, as described above, using a 3 to 48 kHz tone series at 80 to 90 dB SPL. The resulting widefield map was used for localization of low and high frequency borders of A1. For two-photon imaging, mice were head fixed using a custom 3D-printed headbar and placed on a rotating tennis ball under a Bruker Ultima 2P+ two-photon microscope. A 16× Nikon objective (0.8 NA) oriented at 55 to 60 degrees was immersed in ultrasound gel (ParkerLabs Aquasonic CLEAR) and focused to capture low and high frequency regions of layer 2/3 of primary auditory cortex (250 μm deep from cortical surface) using the widefield mapping and local vasculature as a guide. Two-photon excitation was generated by a Chameleon Discovery (Coherent) laser at 920 nm. Precise imaging location was verified by generating a live "Quick Map" of averaged tone evoked responses using 3 frequency stimuli (4, 16, and 64 kHz) presented with 10 repeats at 80 dB SPL, and any adjustments of the imaging field were made to capture both low and high frequency regions of A1 before full dataset acquisition. Acoustic stimulation was generated by an RX6 processor (Tucker Davis Technologies), with 300 ms sinusoidally amplitude-modulated pure tones (4 to 64 kHz, 9 frequencies in ½ octave increments) triggered every 3 s by prespecified frame out signals. Tones were presented in a random order at 30 to 90 dB SPL in 20 dB increments through an electrostatic speaker (ES-1, Tucker Davis Technologies). Images were collected using Prairie View software at 1,024 × 1,024 pixels (1,104 by 1,104 microns) at 15 Hz using an 8 kHz resonant galvanometer.

For analysis of sound-evoked widefield responses, raw widefield epifluorescence images underwent bleach correction and normalization as described above for widefield imaging of spontaneous activity. Image segments were separated by tone frequency, aligned from 1 s prior to and 3 s following tone presentation, and averaged across the 4 presentations of each tone. Normalized and averaged images were used for display purposes. For analysis of evoked amplitude and auditory thresholds in IC, an oval ROI was placed over the contralateral IC. For assessment of spatial band width and frequency mapping, a maximum-intensity projection of the mean sound-evoked response for each presented frequency was rotated by 45 to 55 degrees and a 25 × 250 pixel rectangle was placed along the tonotopic axis, centered at the 3 kHz response location or medial IC location for each animal. To generate the sound-evoked spatial profile, $\Delta F/F_o$ signal intensity was averaged along the short rectangle axis. Profiles were normalized to the maximum $\Delta F/F_o$ intensity (peak response location) along the tonotopic axis. The normalized spatial band width of the evoked response was defined as the width of the 75th percentile of the normalized response for each mouse. For analysis of auditory cortex responses, a circular ROI was placed over A1 after visualization of averaged pure tone responses. The low and high frequency borders of A1 were defined by their caudal and dorsal locations in auditory cortex [52,54]. For calculation of pure tone activation area, normalized images were binarized at a fixed threshold (15% $\Delta F/F_o$) and the total activated area was calculated. Only mice with windows in which the entire auditory cortex was visible were used for analysis. If motion correction was required of widefield movies, it was performed using the MOCO [104] fast motion correction plugin (ImageJ).

For analysis of two-photon sound-evoked calcium imaging, registration, motion correction, and soma ROI identification was performed using Suite2P software [105], and soma and neuropil fluorescence were extracted and imported into MATLAB. Neuropil fluorescence was

subtracted from the soma fluorescence (soma– 0.7 × neuropil) and signals were normalized to their mean baseline values (15 frames (1 s) prior to tone stimulus). Data was unmixed relative to the stimulus presented and averaged to generate mean response traces for all frequency and sound intensity stimuli. Principal component analysis was performed on the peak responses following tone stimuli for all frequency and sound intensity combinations, with the 3 major principal components plotted to demonstrate the distinct response patterns of control and Cx26 cKO cells. Best frequencies were identified as the frequency that elicited the largest calcium response at any sound level. Cells were sorted by their best frequency, and mean evoked responses for each best frequency were plotted at 90 dB SPL. To calculate bandwidth, responsive cells were identified and a single term Gaussian fit ("fit," "Gauss1") applied to the maximum evoked amplitudes at each frequency at 90 dB SPL. Cells were excluded if a Gaussian fit could not be made from the maximum amplitudes.

Statistical analysis

All statistical testing was performed in MATLAB. All data is presented as mean +/− standard deviation, unless otherwise noted. Datasets were tested for normality using the Lilliefors test ("lillietest"). If unable to reject the null hypothesis that the dataset is normally distributed using the Lilliefors test, a paired ("ttest") or unpaired ("ttest2") two-tailed *t* test was used to compare groups. If the null hypothesis of normality was rejected, a nonparametric Wilcoxon rank sum ("ranksum") or Wilcoxon sign rank ("signrank") test was used for unpaired or paired samples, respectively. If multiple comparisons on the same datasets were made, a Benjamini–Hochberg correction of the false discovery rate ("fdr_BH") was made to adjust *p* values to lower the probability of type 1 errors. Comparison of cumulative distributions was performed using a two-sample Kolmogorov–Smirnov test ("kstest2"). Comparison of multiple datasets of independent samples was made using a one-way ANOVA ("anova1") with Tukey's post hoc comparisons. For datasets with multiple comparisons of nonindependent samples, a repeated measures ANOVA ("ranova") or a linear mixed-effects model ("fitlme") were used, using the reduced maximum likelihood fit method ("FitMethod," "reml") and the Satterthwaite approximation of degrees of freedom. Use of a linear mixed model enabled accounting for data dependency for repeated measurements (such as pure tone responses or ABR recordings) from the same mouse as a random effect. Sidák post hoc test was used to assess for post hoc comparisons as indicated in figure legends. Adjusted *p* values are displayed as follows: * = $p < 0.05$, ** = $p < 0.01$, *** = $p < 0.001$, **** = $p < 0.0001$, ns = not significant. Details about number of data points, exact *p* values, and individual statistical tests can be found in the figure legends.

Supporting information

S1 Fig. Morphological anomalies in the organ of Corti with loss of supporting cell Cx26. (a) (Left) Hematoxylin and eosin stain of a P21 control (*Gjb2*$^{fl/fl}$) organ of Corti at high magnification. Hair cell soma are outlined by dashed black lines. (Right) Schematic depicting morphology of hair cells and supporting cells in the control organ of Corti. IPhC, inner phalangeal cell; IPC, inner pillar cell; OPC, outer pillar cell; DCs, Deiters' cells; OHCs, outer hair cells; IHC, inner hair cell. (b) (Left) Hematoxylin and eosin stain of a P21 Cx26 cKO (*Tecta-Cre; Gjb2*$^{fl/fl}$) organ of Corti at high magnification. Hair cell soma are outlined by dashed black lines. (Right) Schematic depicting morphology of hair cells and supporting cells in the Cx26 cKO organ of Corti. Analysis code, plotted figure panels, and statistical analysis can be found at: https://doi.org/10.5281/zenodo.7896212.
(TIF)

S2 Fig. Hair cell degeneration is progressive with increasing age following loss of Cx26. (a) Representative images of hair cells labeled by immunoreactivity to Myosin VIIa (magenta) in whole mounts from apex, middle, and basal regions in control (*Gjb2*$^{fl/fl}$) cochleae at P7, P15, P21, P45, and P100. (b) Representative images of hair cells labeled by immunoreactivity to Myosin VIIa (magenta) in whole mounts from apex, middle, and basal cochlea regions in Cx26 cKO (*Tecta-Cre;Gjb2*$^{fl/fl}$) cochleae at P7, P15, P21, P45, and P100. (c) Quantification of outer hair cells (OHCs, left) and inner hair cells (IHCs, right) with increasing age in apical (squares), middle (diamonds), and basal (circles) regions of control and Cx26 cKO cochlea. Analysis code, plotted figure panels, and statistical analysis can be found at: https://doi.org/10.5281/zenodo.7896212.
(TIF)

S3 Fig. Loss of outer hair cells in Cx26 cKO mice is restricted to basal cochlea at P21. (a) Representative images of hair cells labeled by immunoreactivity to Myosin VIIa (magenta) in whole mounts from apex, middle, and basal cochlea in control (*Gjb2*$^{fl/fl}$, left) and Cx26 cKO (*Tecta-Cre;Gjb2*$^{fl/fl}$, right) mice at P21. White arrows indicate sites of outer hair cell loss. (b) Quantification of inner hair cells (IHCs, left) and outer hair cells (OHCs, right) at P21 in control and Cx26 cKO apical, middle, and basal cochlea segments. $n = 8$ control cochleae, 8 Cx26 cKO cochleae; $p = 0.0974$, 0.0021 (IHCs, OHCs), linear mixed model with Sidák post hoc test. (c) (Left) Low magnification image of SGNs labeled by immunoreactivity to Tuj1 (cyan) in mid-modiolar cross section of P21 cochlea. Labels indicate locations of apical, middle, and basal SGN counts. (Right) Representative high-magnification images of SGN soma labeled by immunoreactivity to Tuj1 in apical, middle, and basal cochlea from control and Cx26 cKO mice at P21. Dashed lines indicate SGN compartment used for area measurement. (d) Quantification of SGN density in apical, middle, and basal cochlea at P21. $n = 3$ control cochleae, 3 Cx26 cKO cochleae; $p = 0.4385$, repeated measures ANOVA with lower bound p value adjustment. Analysis code, plotted figure panels, and statistical analysis can be found at: https://doi.org/10.5281/zenodo.7896212.
(TIF)

S4 Fig. Delayed Cx30 plaque formation in Cx26 cKO inner supporting cells. (a) Immunostaining for Connexin 26 (green) in whole mount middle P7 cochlea from control (*Gjb2*$^{fl/fl}$) and Cx26 cKO (*Tecta-Cre;Gjb2*$^{fl/fl}$) mice. Hair cells (magenta) are labeled by immunoreactivity to Myosin VIIA. (b) Immunostaining for Connexin 26 (green) in mid-turn cochlea cross section at P7. Loss of Cx26 immunostaining is observed in Kölliker's organ and supporting cells of the organ of Corti (white arrows) but not within lateral wall or spiral limbus fibrocytes or the stria vascularis (green arrows). Hair cells are labeled by antibodies against Calbindin (magenta). (c) Immunostaining for Connexin 26 (green) and Connexin 30 (magenta) in whole mount P7 apical organ of Corti from control (top) and Cx26 cKO (bottom) mice. (d) Immunostaining for Connexin 30 (white) in inner supporting cells from whole mount cochlea across increasing developmental age (P7, P12, P21) in control (top) and Cx26 cKO (bottom) mice. (e) Immunostaining for Connexin 30 (magenta) in apical cross section of the organ of Corti at P21. White dashed lines indicate hair cell location. Analysis code, plotted figure panels, and statistical analysis can be found at: https://doi.org/10.5281/zenodo.7896212.
(TIF)

S5 Fig. Loss of Connexin 26 in prehearing supporting cells reduces osmotic crenation size. (a) Intrinsic optical imaging of osmotic crenations in control and Cx26 cKO cochleae. Detected crenations are indicated with transparent colored areas based on time of occurrence. (b) Quantification of spontaneous crenation area. $n = 9$ control, 9 Cx26 cKO cochleae;

p = 4.4669e-4, two-sample t test with unequal variances. Analysis code, plotted figure panels, and statistical analysis can be found at: https://doi.org/10.5281/zenodo.7896212.
(TIF)

S6 Fig. No changes in electrophysiologic properties of immature inner hair cells with loss of Cx26. (a) Schematic of whole cell patch clamp recording from IHCs. (b) Voltage protocol (left) and representative current responses (right) from P7 control (*Gjb2*$^{fl/fl}$) and Cx26 cKO (*Tecta-Cre;Gjb2*$^{fl/fl}$) IHCs. (c) Quantification of membrane resistance and resting membrane potential in P7 control and Cx26 cKO IHCs. n = 13 control, 19 Cx26 cKO; p = 0.9838, 0.9847 (membrane potential, membrane resistance), two-sample t test (membrane potential) or Wilcoxon rank sum test (membrane resistance) with Benjamini–Hochberg correction. Analysis code, plotted figure panels, and statistical analysis can be found at: https://doi.org/10.5281/zenodo.7896212.
(TIF)

S7 Fig. Coordinated activation of future isofrequency lamina in prehearing Cx26 cKO mice. (a) Representative spontaneous neural calcium transients (left) and corresponding normalized spatial fluorescence profile along future tonotopic axis (right, indicated by white rectangle) in IC from P7 control (*Gjb2*$^{fl/fl}$*;Snap25-T2A-GCaMP6s*) mouse. Merged pseudocolored image (bottom) highlights spatial segregation of discrete spontaneous calcium transients. Band width is calculated as the 75th percentile of the normalized spatial profile. (b) Same as (a), but from P7 Cx26 cKO (*Tecta-Cre;Gjb2*$^{fl/fl}$*;Snap25-T2A-GCaMP6s*) mouse. (c) Cumulative distribution of spontaneous event peak location along tonotopic axis of the IC. Gray shading represents central tonotopic region (40th–60th percentile) used for calculation of band width in (e). n = 1,290 control events (7 mice), 1,385 Cx26 cKO events (8 mice); p = 0.4908, two-sample Kolmogorov–Smirnov test. (d) Quantification of spatial integral of all spontaneous events along tonotopic axis. n = 1,290 control events (7 mice), 1,385 Cx26 cKO events (8 mice); p = 1.0825e-9, two-sample Kolmogorov–Smirnov test. (e) (Left) Quantification of mean normalized band width (75th percentile) of spontaneous events along tonotopic axis within central IC. n = 7 control mice, 8 Cx26 cKO mice; p = 0.6620, Wilcoxon rank sum test. (f) Representative spontaneous calcium transients in neurons and neuropil within the inferior colliculus of P7 control (left) and P7 Cx26 cKO (right) mice using two-photon imaging. SR101 (magenta) labels astrocytes for image registration. Normalized fluorescence profile for each event was calculated. (g) (Left) Cumulative distribution of normalized band width of spontaneous calcium transients measured using two-photon imaging. n = 236 control events (5 colliculi, 3 mice), 253 Cx26 cKO events (5 colliculi, 3 mice); p = 0.0059, two-sample Kolmogorov–Smirnov test. (Right) Quantification of mean band width. n = 5 control colliculi (3 mice), 5 Cx26 cKO colliculi (3 mice); p = 0.0958, two-sample t test with unequal variances. Analysis code, plotted figure panels, and statistical analysis can be found at: https://doi.org/10.5281/zenodo.7896212.
(TIF)

S8 Fig. Topographic organization and response amplitudes to tonal stimuli in developing Cx26 cKO mice. (a) Tone-evoked neural calcium transients in IC from P14 control (*Gjb2*$^{fl/fl}$*;Snap25-T2A-GCaMP6s*, left) and P14 Cx26 cKO (*Tecta-Cre;Gjb2*$^{fl/fl}$*;Snap25-T2A-GCaMP6s*, right) mice at 100 dB SPL. Rectangular ROIs were placed along the tonotopic axis of the contralateral IC (low (L) to high (H) frequency), perpendicular to pure tone evoked bands, to determine the peak response location for a pure tone along the tonotopic axis. (b) Quantification of peak response location of pure tones along the tonotopic axis relative to the medial IC. n = 4 control mice, 5 Cx26 cKO mice; mean ± SEM, p = 0.0205, linear mixed effects model. (c)

Quantification of peak response location of pure tones along the tonotopic axis relative to 3 kHz (lowest frequency) peak response location. $n = 4$ control mice, 5 Cx26 cKO mice; mean ± SEM, $p = 0.5654$, linear mixed effects model. (d) Quantification of tone-evoked fluorescence changes in IC within whole IC ROIs across a range of frequency and sound level stimuli in individual P13-P15 control mice. Each black line indicates average responses from the IC contralateral to acoustic stimulation within an individual animal. Vertical gray bar indicates tone presentation. (e) Quantification of tone-evoked fluorescence in IC across a range of frequency and sound level stimuli in individual P13-P15 Cx26 cKO mice. Each red line indicates average responses from the IC contralateral to acoustic stimulation within an individual animal. Vertical gray bar indicates tone presentation. Analysis code, plotted figure panels, and statistical analysis can be found at: https://doi.org/10.5281/zenodo.7896212.
(TIF)

S9 Fig. Auditory dysfunction precedes substantial hair cell degeneration. (a) Average ABR traces to broadband click (left) and 16 kHz tone pip stimuli at multiple sound pressure levels from control (*Gjb2*$^{fl/fl}$, black, $n = 3$) and Cx26 cKO (*Tecta-Cre;Gjb2*$^{fl/fl}$, red, $n = 4$) at P15-P16. Shaded region represents standard deviation of the average signals across animals. (b) Quantification of P15-P16 ABR thresholds to click and pure tone stimuli in controls (*Gjb2*$^{fl/fl}$, black, $n = 3$ and *Tecta-Cre;Gjb2*$^{fl/+}$, blue, $n = 5$) and Cx26 cKO (*Tecta-Cre;Gjb2*$^{fl/fl}$, red, $n = 4$). Detection limit dashed line indicates maximum output from speaker. $p = 4.4717e\text{-}9$ (cKO vs. control), 8.6968e-6 (cKO vs. Cre+ control), 0.1454 (control vs. Cre+ control), linear mixed effects model. (c) Representative images of hair cells labeled by immunoreactivity to Myosin VIIa (magenta) in whole mounts from apex, middle, and basal cochlea in control (*Gjb2*$^{fl/fl}$, left) and Cx26 cKO (*Tecta-Cre;Gjb2*$^{fl/fl}$, right) at P15. White arrows indicate sites of outer hair cell loss. (d) Quantification of inner hair cells (IHCs, left) and outer hair cells (OHCs, right) at P15-P16 in control and Cx26 cKO apical, middle, and basal cochlea segments. $n = 9$ control, 9 Cx26 cKO cochleae; $p = 0.0326$, 0.0053 (IHCs, OHCs), linear mixed model with Sidák post hoc test. (e) (Left) Hematoxylin and eosin stain of a mid-modiolar section of P15 control cochlea. Black square indicates site of high magnification. (Right) Magnified image of the organ of Corti, with the tunnel of Corti indicated by black line. (f) (Left) Hematoxylin and eosin stain of a mid-modiolar section of P15 Cx26 cKO cochlea. Black square indicates site of high magnification. (Right) Magnified image of the organ of Corti, with site of the tunnel of Corti indicated by black line. Analysis code, plotted figure panels, and statistical analysis can be found at: https://doi.org/10.5281/zenodo.7896212.
(TIF)

S1 Video. Inner supporting cells generate spontaneous activity despite absence of Cx26. Confocal imaging of calcium transients in inner hair cells and ISCs in P7 control (*Tecta-Cre;Gjb2*$^{fl/+}$*;R26-lsl-GCaMP3*, top) and Cx26 cKO (*Tecta-Cre;Gjb2*$^{fl/fl}$*;R26-lsl-GCaMP3*, bottom) excised cochlea expressing the genetically encoded calcium indicator GCaMP3. Images were collected at 2 Hz, playback is 10 frames per second.
(MP4)

S2 Video. Spontaneous activity in spiral ganglion neurons is mediated by synaptic glutamate release. Confocal imaging of spontaneous calcium transients in SGNs from an isolated Cx26 cKO (*Tecta-Cre;Gjb2*$^{fl/fl}$*;Snap25-T2A-GCaMP6s*) cochlea. NBQX (50 μm) application eliminates all spontaneous calcium transients. Images were collected at 2 Hz, playback is 20 frames per second.
(MP4)

S3 Video. Preserved spontaneous neural activity in the auditory midbrain of Cx26 cKO mice. Widefield imaging of spontaneous neural activity in the inferior colliculus of P7 control (*Gjb2*$^{fl/fl}$;*Snap25-T2A-GCaMP6s*, top) and Cx26 cKO (*Tecta-Cre;Gjb2*$^{fl/fl}$;*Snap25-T2A-GCaMP6s*, bottom) mice that expressed GCaMP6s pan-neuronally under the *Snap25* promoter. Images were collected at 10 Hz, playback is 20 frames per second.
(MP4)

S4 Video. Tonotopic organization of suprathreshold pure tone responses in Cx26 cKO mice. Widefield imaging of sound-evoked neural activity in the auditory cortex of P14 control (*Gjb2*$^{fl/fl}$;*Snap25-T2A-GCaMP6s*, top) and Cx26 cKO (*Tecta-Cre;Gjb2*$^{fl/fl}$;*Snap25-T2A-GCaMP6s*, bottom) mice, and 3, 12, and 48 kHz sinusoidally amplitude-modulated pure tones are presented for 1 s at 100 dB SPL. Images were collected at 10 Hz, playback is 3 frames per second.
(MP4)

S5 Video. Increased gain of evoked responses after hearing onset in Cx26 cKO mice. Widefield imaging of sound-evoked neural activity in the auditory cortex of P21 control (*Gjb2*$^{fl/fl}$;*Snap25-T2A-GCaMP6s*, left) and Cx26 cKO (*Tecta-Cre;Gjb2*$^{fl/fl}$;*Snap25-T2A-GCaMP6s*, right) mice, and 3, 16, and 48 kHz sinusoidally amplitude-modulated pure tones are presented for 1 s at 100 dB SPL. Images were collected at 10 Hz, playback is 3 frames per second.
(MP4)

S6 Video. Increased engagement of cortical neurons to suprathreshold acoustic stimuli in Cx26 cKO mice. Two-photon imaging of sound-evoked neural activity in the auditory cortex of P21 control (*Gjb2*$^{fl/fl}$;*Snap25-T2A-GCaMP6s*, left) and Cx26 cKO (*Tecta-Cre;Gjb2*$^{fl/fl}$;*Snap25-T2A-GCaMP6s*, right) mice, and 3, 12, and 48 kHz sinusoidally amplitude-modulated pure tones are presented for 0.3 s at 90 dB SPL. Images were collected at 15 Hz, playback is 4 frames per second.
(MP4)

Acknowledgments

We thank members of the Bergles laboratory for discussions and comments on the manuscript. We thank Michele Pucak and Abigail Bush in the Multiphoton Imaging Core and Terry Shelley in the Neuroscience Machine Shop for assistance.

Author Contributions

Conceptualization: Calvin J. Kersbergen, Dwight E. Bergles.

Data curation: Calvin J. Kersbergen, Travis A. Babola.

Formal analysis: Calvin J. Kersbergen, Travis A. Babola.

Funding acquisition: Calvin J. Kersbergen, Travis A. Babola, Patrick O. Kanold, Dwight E. Bergles.

Investigation: Calvin J. Kersbergen, Travis A. Babola.

Methodology: Calvin J. Kersbergen, Dwight E. Bergles.

Project administration: Calvin J. Kersbergen, Dwight E. Bergles.

Resources: Calvin J. Kersbergen, Travis A. Babola, Patrick O. Kanold, Dwight E. Bergles.

Software: Calvin J. Kersbergen, Travis A. Babola.

Supervision: Calvin J. Kersbergen, Dwight E. Bergles.

Visualization: Dwight E. Bergles.

Writing – original draft: Calvin J. Kersbergen, Dwight E. Bergles.

Writing – review & editing: Calvin J. Kersbergen, Travis A. Babola, Patrick O. Kanold, Dwight E. Bergles.

References

1. Monzack EL, Cunningham LL. Lead roles for supporting actors: Critical functions of inner ear supporting cells. Hear Res. 2013; 303:20–29. https://doi.org/10.1016/j.heares.2013.01.008 PMID: 23347917
2. Wan G, Corfas G, Stone JS. Inner ear supporting cells: Rethinking the silent majority. Semin Cell Dev Biol. 2013; 24(5):448–459. https://doi.org/10.1016/j.semcdb.2013.03.009 PMID: 23545368
3. Jagger DJ, Forge A. Compartmentalized and Signal-Selective Gap Junctional Coupling in the Hearing Cochlea. J Neurosci. 2006; 26(4):1260–1268. https://doi.org/10.1523/JNEUROSCI.4278-05.2006 PMID: 16436613
4. Kikuchi T, Kimura RS, Paul DL, Adams JC. Gap junctions in the rat cochlea: immunohistochemical and ultrastructural analysis. Anat Embryol. 1995; 191(2):101–118. https://doi.org/10.1007/BF00186783 PMID: 7726389
5. Santos-Sacchi J, Dallos P. Intercellular communication in the supporting cells of the organ of Corti. Hear Res. 1983; 9(3):317–326. https://doi.org/10.1016/0378-5955(83)90034-5 PMID: 6841286
6. Liu W, Boström M, Kinnefors A, Rask-Andersen H. Unique expression of connexins in the human cochlea. Hear Res. 2009; 250(1–2):55–62. https://doi.org/10.1016/j.heares.2009.01.010 PMID: 19450429
7. Zdebik AA, Wangemann P, Jentsch TJ. Potassium ion movement in the inner ear: Insights from genetic disease and mouse models. Phys Ther. 2009; 24(5):307–316. https://doi.org/10.1152/physiol.00018.2009 PMID: 19815857
8. Kelsell DP, Dunlop J, Stevens HP, Lench NJ, Liang JN, Parry G, et al. Connexin 26 mutations in hereditary non-syndromic sensorineural deafness. Nature. 1997; 387:80–83. https://doi.org/10.1038/387080a0 PMID: 9139825
9. Chan DK, Chang KW. GJB2-associated hearing loss: Systematic review of worldwide prevalence, genotype, and auditory phenotype. Laryngoscope. 2014; 124(2):34–53. https://doi.org/10.1002/lary.24332 PMID: 23900770
10. Del Castillo FJ, Del Castillo I. DFNB1 non-syndromic hearing impairment: Diversity of mutations and associated phenotypes. Front Mol Neurosci. 2017: 10. https://doi.org/10.3389/fnmol.2017.00428 PMID: 29311818
11. Cohen-Salmon M, Ott T, Michel V, Hardelin JP, Perfettini I, Eybalin M, et al. Targeted ablation of connexin26 in the inner ear epithelial gap junction network causes hearing impairment and cell death. Curr Biol. 2002; 12(13):1106–1111. https://doi.org/10.1016/s0960-9822(02)00904-1 PMID: 12121617
12. Wang Y, Chang Q, Tang W, Sun Y, Zhou B, Li H, et al. Targeted connexin26 ablation arrests postnatal development of the organ of Corti. Biochem Biophys Res Commun. 2009; 385(1):33–37. https://doi.org/10.1016/j.bbrc.2009.05.023 PMID: 19433060
13. Snoeckx RL, Huygen PLM, Feldmann D, Marlin S, Denoyelle F, Waligora J, et al. GJB2 mutations and degree of hearing loss: A multicenter study. Am J Hum Genet. 2005; 77(6):945–957. https://doi.org/10.1086/497996 PMID: 16380907
14. Burke WF, Warnecke A, Schöner-Heinisch A, Lesinski-Schiedat A, Maier H, Lenarz T. Prevalence and audiological profiles of GJB2 mutations in a large collective of hearing impaired patients. Hear Res. 2016; 333:77–86. https://doi.org/10.1016/j.heares.2016.01.006 PMID: 26778469
15. Jun AI, McGuirt WT, Hinojosa R, Green GE, Fischel-Ghodsian N, Smith RJH. Temporal bone histopathology in connexin 26-related hearing loss. Laryngoscope. 2000; 110(2):269. https://doi.org/10.1097/00005537-200002010-00016 PMID: 10680928
16. Wu CM, Ko HC, Tsou YT, Lin YH, Lin JL, Chen CK, et al. Long-term cochlear implant outcomes in children with GJB2 and SLC26A4 mutations. PLoS ONE. 2015; 10(9). https://doi.org/10.1371/journal.pone.0138575 PMID: 26397989
17. Kirkby LA, Sack GS, Firl A, Feller MB. A role for correlated spontaneous activity in the assembly of neural circuits. Neuron. 2013; 80(5):1129–1144. https://doi.org/10.1016/j.neuron.2013.10.030 PMID: 24314725

18. Tritsch NX, Yi E, Gale JE, Glowatzki E, Bergles DE. The origin of spontaneous activity in the developing auditory system. Nature. 2007; 450:50–55. https://doi.org/10.1038/nature06233 PMID: 17972875

19. Wang HC, Lin CC, Cheung R, Zhang-Hooks Y, Agarwal A, Ellis-Davies G, et al. Spontaneous Activity of Cochlear Hair Cells Triggered by Fluid Secretion Mechanism in Adjacent Support Cells. Cell. 2015; 163(6):1348–1359. https://doi.org/10.1016/j.cell.2015.10.070 PMID: 26627734

20. Sonntag M, Englitz B, Kopp-Scheinpflug C, Rübsamen R. Early postnatal development of spontaneous and acoustically evoked discharge activity of principal cells of the medial nucleus of the trapezoid body: An in vivo study in mice. J Neurosci. 2009; 29(30):9510–9520. https://doi.org/10.1523/JNEUROSCI.1377-09.2009 PMID: 19641114

21. Tritsch NX, Rodríguez-Contreras A, Crins TTH, Wang HC, Borst JGG, Bergles DE. Calcium action potentials in hair cells pattern auditory neuron activity before hearing onset. Nat Neurosci. 2010; 13 (9):1050–1052. https://doi.org/10.1038/nn.2604 PMID: 20676105

22. Babola TA, Li S, Gribizis A, Lee BJ, Issa JB, Wang HC, et al. Homeostatic Control of Spontaneous Activity in the Developing Auditory System. Neuron. 2018; 99(3):511–524. https://doi.org/10.1016/j.neuron.2018.07.004 PMID: 30077356

23. Clause A, Kim G, Sonntag M, Weisz CJC, Vetter DE, Rubsamen R, et al. The Precise Temporal Pattern of Prehearing Spontaneous Activity Is Necessary for Tonotopic Map Refinement. Neuron. 2014; 82(4):822–835. https://doi.org/10.1016/j.neuron.2014.04.001 PMID: 24853941

24. Blankenship AG, Feller MB. Mechanisms underlying spontaneous patterned activity in developing neural circuits. Nat Rev Neurosci. 2010; 11(1):18–29. https://doi.org/10.1038/nrn2759 PMID: 19953103

25. Ge X, Zhang K, Gribizis A, Hamodi AS, Sabino AM, Crair MC. Retinal waves prime visual motion detection by simulating future optic flow. Science. 2021; 373:1–10. https://doi.org/10.1126/science.abd0830 PMID: 34437090

26. Anselmi F, Hernandez VH, Crispino G, Seydel A, Ortolano S, Roper SD, et al. ATP release through connexin hemichannels and gap junction transfer of second messengers propagate Ca2+ signals across the inner ear. Proc Natl Acad Sci U S A. 2008; 105(48):18770–18775. https://doi.org/10.1073/pnas.0800793105 PMID: 19047635

27. Zhao HB, Yu N, Fleming CR. Gap junctional hemichannel-mediated ATP release and hearing controls in the inner ear. Proc Natl Acad Sci U S A. 2005; 102(51):18724–18729. https://doi.org/10.1073/pnas.0506481102 PMID: 16344488

28. Gabriel HD, Jung D, Bützler C, Temme A, Traub O, Winterhager E, et al. Transplacental uptake of glucose is decreased in embryonic lethal connexin26-deficient mice. J Cell Biol. 1998; 140(6):1453–1461. https://doi.org/10.1083/jcb.140.6.1453 PMID: 9508777

29. Beltramello M, Piazza V, Bukauskas FF, Pozzan T, Mammano F. Impaired permeabilty to Ins(1,4,5)P3 in a mutant connexin underlies recessive hereditary deafness. Nat Cell Biol. 2005; 7(1):63–69.

30. Chang Q, Tang W, Ahmad S, Zhou B, Lin X. Gap junction mediated intercellular metabolite transfer in the cochlea is compromised in connexin30 null mice. PLoS ONE. 2008; 3(12). https://doi.org/10.1371/journal.pone.0004088 PMID: 19116647

31. Zhang Y, Tang W, Ahmad S, Sipp JA, Chen P, Lin X. Gap junction-mediated intercellular biochemical coupling in cochlear supporting cells is required for normal cochlear functions. Proc Natl Acad Sci U S A. 2005; 102(42):15201–15206. https://doi.org/10.1073/pnas.0501859102 PMID: 16217030

32. Babola TA, Kersbergen CJ, Wang HC, Bergles DE. Purinergic signaling in cochlear supporting cells reduces hair cell excitability by increasing the extracellular space. Elife. 2020; 9:1–30. https://doi.org/10.7554/eLife.52160 PMID: 31913121

33. Kersbergen CJ, Babola TA, Rock J, Bergles DE. Developmental spontaneous activity promotes formation of sensory domains, frequency tuning and proper gain in central auditory circuits. Cell Rep. 2022; 41(7):111649. https://doi.org/10.1016/j.celrep.2022.111649 PMID: 36384119

34. Rau A, Legan KP, Richardson GP. Tectorin mRNA expression is spatially and temporally restricted during mouse inner ear development. J Comp Neurol. 1999; 405(2):271–280. PMID: 10023815

35. Crispino G, Di Pasquale G, Scimemi P, Rodriguez L, Ramirez FG, de Siati RD, et al. BAAV mediated GJB2 gene transfer restores gap junction coupling in cochlear organotypic cultures from deaf Cx26Sox10Cre mice. PLoS ONE. 2011; 6(8). https://doi.org/10.1371/journal.pone.0023279 PMID: 21876744

36. Sun Y, Tang W, Chang Q, Wang Y, Kong W, Lin X. Connexin30 null and conditional connexin26 null mice display distinct pattern and time course of cellular degeneration in the cochlea. J Comp Neurol. 2009; 516(6):569–579. https://doi.org/10.1002/cne.22117 PMID: 19673007

37. Chang Q, Tang W, Kim Y, Lin X. Timed conditional null of connexin26 in mice reveals temporary requirements of connexin26 in key cochlear developmental events before the onset of hearing. Neurobiol Dis. 2015; 73:418–427. https://doi.org/10.1016/j.nbd.2014.09.005 PMID: 25251605

38. Teubner B, Michel V, Pesch J, Lautermann J, Cohen-Salmon M, Söhl G, et al. Connexin30 (Gjb6)-deficiency causes severe hearing impairment and lack of endocochlear potential. Hum Mol Genet. 2003; 12(1):13–21. https://doi.org/10.1093/hmg/ddg001 PMID: 12490528

39. Kamiya K, Yum SW, Kurebayashi N, Muraki M, Ogawa K, Karasawa K, et al. Assembly of the cochlear gap junction macromolecular complex requires connexin 26. J Clin Invest. 2014; 124(4):1598–1607. https://doi.org/10.1172/JCI67621 PMID: 24590285

40. Ortolano S, Di Pasquale G, Crispino G, Anselmi F, Mammano F, Chiorini JA. Coordinated control of connexin 26 and connexin 30 at the regulatory and functional level in the inner ear. Proc Natl Acad Sci U S A. 2008; 105(48):18776–18781. https://doi.org/10.1073/pnas.0800831105 PMID: 19047647

41. Tritsch NX, Bergles DE. Developmental regulation of spontaneous activity in the mammalian cochlea. J Neurosci. 2010; 30(4):1539–1550. https://doi.org/10.1523/JNEUROSCI.3875-09.2010 PMID: 20107081

42. Babola TA, Li S, Wang Z, Kersbergen CJ, Elgoyhen AB, Coate TM, et al. Purinergic signaling controls spontaneous activity in the auditory system throughout early development. J Neurosci. 2021; 41 (4):594–612. https://doi.org/10.1523/JNEUROSCI.2178-20.2020 PMID: 33303678

43. Rodriguez L, Simeonato E, Scimemi P, Anselmi F, Calì B, Crispino G, et al. Reduced phosphatidylinositol 4,5-bisphosphate synthesis impairs inner ear Ca2+ signaling and high-frequency hearing acquisition. Proc Natl Acad Sci U S A. 2012; 109(35):14013–14018. https://doi.org/10.1073/pnas.1211869109 PMID: 22891314

44. Ceriani F, Hendry A, Jeng J, Johnson SL, Stephani F, Olt J, et al. Coordinated calcium signalling in cochlear sensory and non-sensory cells refines afferent innervation of outer hair cells. EMBO J. 2019; 38(9):1–19. https://doi.org/10.15252/embj.201899839 PMID: 30804003

45. Paukert M, Agarwal A, Cha J, Doze VA, Kang JU, Bergles DE. Norepinephrine controls astroglial responsiveness to local circuit activity. Neuron. 2014 Jun 18; 82(6):1263–70. https://doi.org/10.1016/j.neuron.2014.04.038 PMID: 24945771

46. Zhang-Hooks YX, Agarwal A, Mishina M, Bergles DE. NMDA Receptors Enhance Spontaneous Activity and Promote Neuronal Survival in the Developing Cochlea. Neuron. 2016; 89(2):337–350. https://doi.org/10.1016/j.neuron.2015.12.016 PMID: 26774161

47. Madisen L, Garner AR, Shimaoka D, Chuong AS, Klapoetke NC, Li L, et al. Transgenic mice for intersectional targeting of neural sensors and effectors with high specificity and performance. Neuron. 2015; 85(5):942–958. https://doi.org/10.1016/j.neuron.2015.02.022 PMID: 25741722

48. Sun S, Babola T, Pregernig G, So KS, Nguyen M, Su SSM, et al. Hair Cell Mechanotransduction Regulates Spontaneous Activity and Spiral Ganglion Subtype Specification in the Auditory System. Cell. 2018; 174(5):1247–1263. https://doi.org/10.1016/j.cell.2018.07.008 PMID: 30078710

49. Tong L, Strong MK, Kaur T, Juiz JM, Oesterle EC, Hume C, et al. Selective deletion of cochlear hair cells causes rapid age-dependent changes in spiral ganglion and cochlear nucleus neurons. J Neurosci. 2015; 35(20):7878–7891. https://doi.org/10.1523/JNEUROSCI.2179-14.2015 PMID: 25995473

50. Shrestha BR, Chia C, Wu L, Kujawa SG, Liberman MC, Goodrich LV. Sensory Neuron Diversity in the Inner Ear Is Shaped by Activity. Cell. 2018; 174(5):1229–1246. https://doi.org/10.1016/j.cell.2018.07.007 PMID: 30078709

51. Wang Y, Sanghvi M, Gribizis A, Zhang Y, Song L, Morley B, et al. Efferent feedback controls bilateral auditory spontaneous activity. Nat Commun. 2021; 12(2449). https://doi.org/10.1038/s41467-021-22796-8 PMID: 33907194

52. Romero S, Hight AE, Clayton KK, Resnik J, Williamson RS, Hancock KE, et al. Cellular and Widefield Imaging of Sound Frequency Organization in Primary and Higher Order Fields of the Mouse Auditory Cortex. Cereb Cortex. 2020; 30(3):1603–1622. https://doi.org/10.1093/cercor/bhz190 PMID: 31667491

53. Kanold PO, Nelken I, Polley DB. Local versus global scales of organization in auditory cortex. Trends Neurosci. 2014; 37:502–510. https://doi.org/10.1016/j.tins.2014.06.003 PMID: 25002236

54. Issa JB, Haeffele BD, Agarwal A, Bergles DE, Young ED, Yue DT. Multiscale Optical Ca2+ Imaging of Tonal Organization in Mouse Auditory Cortex. Neuron. 2014; 83(4):944–959. https://doi.org/10.1016/j.neuron.2014.07.009 PMID: 25088366

55. Meng X, Solarana K, Bowen Z, Liu J, Nagode DA, Sheikh A, et al. Transient Subgranular Hyperconnectivity to L2/3 and Enhanced Pairwise Correlations During the Critical Period in the Mouse Auditory Cortex. Cereb Cortex. 2020; 30(3):1914–1930. https://doi.org/10.1093/cercor/bhz213 PMID: 31667495

56. Kellner V, Kersbergen CJ, Li S, Babola TA, Saher G, Bergles DE. Dual metabotropic glutamate receptor signaling enables coordination of astrocyte and neuron activity in developing sensory domains. Neuron. 2021; 109(16):2545–2555. https://doi.org/10.1016/j.neuron.2021.06.010 PMID: 34245686

57. De Villers-Sidani E, Chang EF, Bao S, Merzenich MM. Critical period window for spectral tuning defined in the primary auditory cortex (A1) in the rat. J Neurosci. 2007; 27(1):180–189. https://doi.org/10.1523/JNEUROSCI.3227-06.2007 PMID: 17202485

58. Chang EF, Merzenich MM. Environmental Noise Retards Auditory Cortical Development. Science. 2003; 300:498–502. https://doi.org/10.1126/science.1082163 PMID: 12702879

59. Zhang LI, Bao S, Merzenich MM. Persistent and specific influences of early acoustic environments on primary auditory cortex. Nat Neurosci. 2001; 4(11):1123–1130. https://doi.org/10.1038/nn745 PMID: 11687817

60. Dorrn AL, Yuan K, Barker AJ, Schreiner CE, Froemke RC. Developmental sensory experience balances cortical excitation and inhibition. Nature. 2010; 465:932–936. https://doi.org/10.1038/nature09119 PMID: 20559387

61. Sun YJ, Wu GK, Liu BH, Li P, Zhou M, Xiao Z, et al. Fine-tuning of pre-balanced excitation and inhibition during auditory cortical development. Nature. 2010; 465:927–931. https://doi.org/10.1038/nature09079 PMID: 20559386

62. Nishio SY, Usami SI. Outcomes of cochlear implantation for the patients with specific genetic etiologies: a systematic literature review. Acta Otolaryngol. 2017; 137(7):730–742. https://doi.org/10.1080/00016489.2016.1276303 PMID: 28498079

63. Abdurehim Y, Lehmann A, Zeitouni AG. Predictive Value of GJB2 Mutation Status for Hearing Outcomes of Pediatric Cochlear Implantation. Otolaryngol Neck Surg. 2017; 157(1):16–24. https://doi.org/10.1177/0194599817697054 PMID: 28322114

64. Zhu Y, Zong L, Mei L, Zhao HB. Connexin26 gap junction mediates miRNA intercellular genetic communication in the cochlea and is required for inner ear development. Sci Rep. 2015; 5:1–8. https://doi.org/10.1038/srep15647 PMID: 26490746

65. Piazza V, Ciubotaru CD, Gale JE, Mammano F. Purinergic signalling and intercellular Ca2+ wave propagation in the organ of Corti. Cell Calcium. 2007; 41(1):77–86. https://doi.org/10.1016/j.ceca.2006.05.005 PMID: 16828497

66. Jagger DJ, Forge A. Connexins and gap junctions in the inner ear–it's not just about K+ recycling. Cell Tissue Res. 2015; 360(3):633–644.

67. Forge A, Becker D, Casalotti S, Edwards J, Marziano N, Nevill G. Gap Junctions in the Inner Ear: Comparison of Distribution Patterns in Different Vertebrates and Assessment of Connexin Composition in Mammals. J Comp Neurol. 2003; 467(2):207–231.

68. Lautermann J, Ten Cate WJF, Altenhoff P, Grümmer R, Traub O, Frank HG, et al. Expression of the gap-junction connexins 26 and 30 in the rat cochlea. Cell Tissue Res. 1998; 294(3):415–420. https://doi.org/10.1007/s004410051192 PMID: 9799458

69. Boulay A-C, del Castillo FJ, Giraudet F, Hamard G, Giaume C, Petit C, et al. Hearing Is Normal without Connexin30. J Neurosci. 2013; 33(2):430–434. https://doi.org/10.1523/JNEUROSCI.4240-12.2013 PMID: 23303923

70. Kolla L, Kelly MC, Mann ZF, Anaya-Rocha A, Ellis K, Lemons A, et al. Characterization of the development of the mouse cochlear epithelium at the single cell level. Nat Commun. 2020; 11(1). https://doi.org/10.1038/s41467-020-16113-y PMID: 32404924

71. Kubota M, Scheibinger M, Jan TA, Heller S. Greater epithelial ridge cells are the principal organoid-forming progenitors of the mouse cochlea. Cell Rep. 2021 Jan 19; 34(3). https://doi.org/10.1016/j.celrep.2020.108646 PMID: 33472062

72. Cohen-Salmon M, Maxeiner S, Krüger O, Theis M, Willecke K, Petit C. Expression of the connexin43- and connexin45-encoding genes in the developing and mature mouse inner ear. Cell Tissue Res. 2004; 316(1):15–22. https://doi.org/10.1007/s00441-004-0861-2 PMID: 14986102

73. Cotrina ML, Lin JHC, Alves-Rodrigues A, Liu S, Li J, Azmi-Ghadimi H, et al. Connexins regulate calcium signaling by controlling ATP release. Proc Natl Acad Sci U S A. 1998; 95(26):15735–15740. https://doi.org/10.1073/pnas.95.26.15735 PMID: 9861039

74. Johnson SL, Ceriani F, Houston O, Polishchuk R, Polishchuk E, Crispino G, et al. Connexin-Mediated Signaling in Nonsensory Cells Is Crucial for the Development of Sensory Inner Hair Cells in the Mouse Cochlea. J Neurosci. 2017; 37(2):258–268. https://doi.org/10.1523/JNEUROSCI.2251-16.2016 PMID: 28077706

75. Zorzi V, Paciello F, Ziraldo G, Peres C, Mazzarda F, Nardin C, et al. Mouse Panx1 is dispensable for hearing acquisition and auditory function. Front Mol Neurosci. 2017: 10. https://doi.org/10.3389/fnmol.2017.00379 PMID: 29234270

76. Eckrich T, Blum K, Milenkovic I, Engel J. Fast Ca2+ Transients of Inner Hair Cells Arise Coupled and Uncoupled to Ca2+ Waves of Inner Supporting Cells in the Developing Mouse Cochlea. Front Mol Neurosci. 2018: 11. https://doi.org/10.3389/fnmol.2018.00264 PMID: 30104958

77. Maul A, Huebner AK, Strenzke N, Moser T, Rübsamen R, Jovanovic S, et al. The Cl—channel TMEM16A is involved in the generation of cochlear Ca2+ waves and promotes the refinement of auditory brainstem networks in mice. Elife. 2022; 11:72251.

78. Kotak VC, Fujisawa S, Lee FA, Karthikeyan O, Aoki C, Sanes DH. Hearing loss raises excitability in the auditory cortex. J Neurosci. 2005; 25(15):3908–3918. https://doi.org/10.1523/JNEUROSCI.5169-04.2005 PMID: 15829643

79. Kotak VC, Takesian AE, Sanes DH. Hearing loss prevents the maturation of GABAergic transmission in the auditory cortex. Cereb Cortex. 2008; 18(9):2098–2108. https://doi.org/10.1093/cercor/bhm233 PMID: 18222937

80. Chambers AR, Resnik J, Yuan Y, Whitton JP, Edge AS, Liberman MC, et al. Central Gain Restores Auditory Processing following Near-Complete Cochlear Denervation. Neuron. 2016; 89(4):867–879. https://doi.org/10.1016/j.neuron.2015.12.041 PMID: 26833137

81. Mowery TM, Kotak VC, Sanes DH. Transient Hearing Loss Within a Critical Period Causes Persistent Changes to Cellular Properties in Adult Auditory Cortex. Cereb Cortex. 2015; 25(8):2083–2094. https://doi.org/10.1093/cercor/bhu013 PMID: 24554724

82. Resnik J, Polley DB. Cochlear neural degeneration disrupts hearing in background noise by increasing auditory cortex internal noise. Neuron. 2021; 109(6):984–996. https://doi.org/10.1016/j.neuron.2021.01.015 PMID: 33561398

83. Seki S, Eggermont JJ. Changes in spontaneous firing rate and neural synchrony in cat primary auditory cortex after localized tone-induced hearing loss. Hear Res. 2003; 180(1–2):28–38. https://doi.org/10.1016/s0378-5955(03)00074-1 PMID: 12782350

84. Kral A, Tillein J, Heid S, Hartmann R, Klinke R. Postnatal Cortical Development in Congenital Auditory Deprivation. Cereb Cortex. 2005; 15(5):552–562. https://doi.org/10.1093/cercor/bhh156 PMID: 15319310

85. McGill M, Hight AE, Watanabe YL, Parthasarathy A, Cai D, Clayton K, et al. Neural signatures of auditory hypersensitivity following acoustic trauma. Elife. 2022; 11:80015. https://doi.org/10.7554/eLife.80015 PMID: 36111669

86. Resnik J, Polley DB. Fast-spiking GABA circuit dynamics in the auditory cortex predict recovery of sensory processing following peripheral nerve damage. Elife. 2017; 6:21452. https://doi.org/10.7554/eLife.21452 PMID: 28323619

87. Balaram P, Hackett TA, Polley DB. Synergistic Transcriptional Changes in AMPA and GABAA Receptor Genes Support Compensatory Plasticity Following Unilateral Hearing Loss. Neuroscience. 2019; 407:108–119. https://doi.org/10.1016/j.neuroscience.2018.08.023 PMID: 30176318

88. Auerbach BD, Rodrigues PV, Salvi RJ. Central Gain Control in Tinnitus and Hyperacusis. Front Neurol. 2014; 5(206). https://doi.org/10.3389/fneur.2014.00206 PMID: 25386157

89. Shore SE, Roberts LE, Langguth B. Maladaptive plasticity in tinnitus—triggers, mechanisms and treatment. Nat Rev Neurol. 2016; 12(3):150–160. https://doi.org/10.1038/nrneurol.2016.12 PMID: 26868680

90. Yang S, Weiner BD, Zhang LS, Cho SJ, Bao S. Homeostatic plasticity drives tinnitus perception in an animal model. Proc Natl Acad Sci U S A. 2011; 108(36):14974–14979. https://doi.org/10.1073/pnas.1107998108 PMID: 21896771

91. Zeng FG. An active loudness model suggesting tinnitus as increased central noise and hyperacusis as increased nonlinear gain. Hear Res. 2013 Jan 1; 295:172–9. https://doi.org/10.1016/j.heares.2012.05.009 PMID: 22641191

92. Eggermont JJ, Kral A. Somatic memory and gain increase as preconditions for tinnitus: Insights from congenital deafness. Hear Res. 2016 Mar 1; 333:37–48. https://doi.org/10.1016/j.heares.2015.12.018 PMID: 26719143

93. Roberts LE, Eggermont JJ, Caspary DM, Shore SE, Melcher JR, Kaltenbach JA. Ringing Ears: The Neuroscience of Tinnitus. J Neurosci. 2010; 30(45):14972–14979. https://doi.org/10.1523/JNEUROSCI.4028-10.2010 PMID: 21068300

94. Olze H, Szczepek AJ, Haupt H, Förster U, Zirke N, Gräbel S, et al. Cochlear implantation has a positive influence on quality of life, tinnitus, and psychological comorbidity. Laryngoscope. 2011; 121(10):2220–2227. https://doi.org/10.1002/lary.22145 PMID: 21898434

95. Baguley DM, Atlas MD. Cochlear implants and tinnitus. Prog Brain Res. 2007; 166:347–355. https://doi.org/10.1016/S0079-6123(07)66033-6 PMID: 17956799

96. Liberman MC, Gao J, He DZZ, Wu X, Jia S, Zuo J. Prestin is required for electromotility of the outer hair cell and for the cochlear amplifier. Nature. 2002; 419:300–304. https://doi.org/10.1038/nature01059 PMID: 12239568

97. Mellado Lagarde MM, Cox BC, Fang J, Taylor R, Forge A, Zuo J. Selective ablation of pillar and deiters' cells severely affects cochlear postnatal development and hearing in mice. J Neurosci. 2013; 33 (4):1564–1576. https://doi.org/10.1523/JNEUROSCI.3088-12.2013 PMID: 23345230

98. Lukashkina VA, Yamashita T, Zuo J, Lukashkin AN, Russell IJ. Amplification mode differs along the length of the mouse cochlea as revealed by connexin 26 deletion from specific gap junctions. Sci Rep. 2017; 7(1):1–11.

99. Zhu Y, Liang C, Chen J, Zong L, Di CG, Zhao HB. Active cochlear amplification is dependent on supporting cell gap junctions. Nat Commun. 2013; 4:1786–1788. https://doi.org/10.1038/ncomms2806 PMID: 23653198

100. McGovern MM, Brancheck J, Grant AC, Graves KA, Cox BC. Quantitative Analysis of Supporting Cell Subtype Labeling Among CreER Lines in the Neonatal Mouse Cochlea. JARO—J Assoc Res Otolaryngol. 2017; 18(2):227–245. https://doi.org/10.1007/s10162-016-0598-0 PMID: 27873085

101. Kudo T, Kure S, Ikeda K, Xia AP, Katori Y, Suzuki M, et al. Transgenic expression of a dominant-negative connexin26 causes degeneration of the organ of Corti and non-syndromic deafness. Hum Mol Genet. 2003; 12(9):995–1004. https://doi.org/10.1093/hmg/ddg116 PMID: 12700168

102. Sousa VH, Miyoshi G, Hjerling-Leffler J, Karayannis T, Fishell G. Characterization of Nkx6-2-derived neocortical interneuron lineages. Cereb Cortex. 2009; 19:1–10.

103. Kim YH, Schrode KM, Engel J, Vicencio-Jimenez S, Rodriguez G, Lee HK, et al. Auditory Behavior in Adult-Blinded Mice. JARO—J Assoc Res Otolaryngol. 2022; 23(2):225–239. https://doi.org/10.1007/s10162-022-00835-5 PMID: 35084628

104. Dubbs A, Guevara J, Yuste R. moco: Fast Motion Correction for Calcium Imaging. Front Neuroinform. 2016; 10(6). https://doi.org/10.3389/fninf.2016.00006 PMID: 26909035

105. Pachitariu M, Stringer C, Dipoppa M, Schröder S, Rossi LF, Dalgleish H, et al. Suite2p: beyond 10,000 neurons with standard two-photon microscopy. bioRxiv. 2017:061507.